JGR Atmospheres

RESEARCH ARTICLE
10.1029/2021JD035990

This article is a companion to Fritts et al. (2022), https://doi.org/10.1029/2021JD036035.

Key Points:

- Simulations of mountain wave (MW) dynamics reveal decreasing fidelity in MW and large-scale fields at degraded resolution
- Two-km resolution or better yields reasonable fidelity to MW fields, momentum fluxes, and large-scale fields into the mesosphere
- Four-km resolution fails to capture realistic MWs, fluxes, and responses; 8 km resolution yields no resemblance to well-resolved MW fields

Supporting Information:

Supporting Information may be found in the online version of this article.

Correspondence to:

D. C. Fritts,
dave@gats-inc.com

Citation:

Fritts, D. C., Lund, A. C., Lund, T. S., & Yudin, V. (2022). Impacts of limited model resolution on the representation of mountain wave and secondary gravity wave dynamics in local and global models. 1: Mountain waves in the stratosphere and mesosphere. *Journal of Geophysical Research: Atmospheres*, *127*, e2021JD035990. https://doi.org/10.1029/2021JD035990

Received 12 OCT 2021
Accepted 14 FEB 2022

Author Contributions:

Conceptualization: David C. Fritts
Funding acquisition: David C. Fritts
Methodology: Adam C. Lund, Thomas S. Lund
Software: Thomas S. Lund
Validation: Thomas S. Lund

Impacts of Limited Model Resolution on the Representation of Mountain Wave and Secondary Gravity Wave Dynamics in Local and Global Models. 1: Mountain Waves in the Stratosphere and Mesosphere

David C. Fritts[1,2], Adam C. Lund[2], Thomas S. Lund[1,3], and Valery Yudin[4]

[1]GATS, Boulder, CO, USA, [2]Embry-Riddle Aeronautical University, Daytona Beach, FL, USA, [3]University of Colorado Boulder, Boulder, CO, USA, [4]Catholic University of America, Washington, DC, USA

Abstract Long-term efforts have sought to extend global model resolution to smaller scales enabling more accurate descriptions of gravity wave (GW) sources and responses, given their major roles in coupling and variability throughout the atmosphere. Such studies reveal significant improvements accompanying increasing resolution, but no guidance on what is sufficient to approximate reality. We take the opposite approach, using a finite-volume model solving the Navier-Stokes equations exactly. The reference simulation addresses mountain wave (MW) generation and responses over the Southern Andes described using isotropic 500 m, central resolution by Fritts et al. (2021), https://doi.org/10.1175/JAS-D-20-0207.1 and Lund et al. (2020), https://doi.org/10.1175/JAS-D-19-0356.1. Reductions of horizontal resolution to 1 and 2 km result in (a) systematic increases in initial MW breaking altitudes, (b) weaker, larger-scale generation of secondary GWs and acoustic waves accompanying these dynamics, and (c) significantly weaker and less extended responses in the mesosphere in latitude and longitude. Horizontal resolution of 4 km largely suppresses instabilities, but allows weak, sustained mean-flow interactions. Responses for 8 km resolution are very weak and fail to capture any aspects of the high-resolution responses. The chosen mean winds allow efficient MW penetration into the mesosphere and lower thermosphere, hence only exhibit strong pseudo-momentum deposition and mean wind decelerations at higher altitudes. A companion paper by Fritts et al. (2022), https://doi.org/10.1029/2021JD036035 explores the impacts of decreasing resolution on responses in the thermosphere.

Plain Language Summary Mountain waves play major roles in the large-scale circulation and structure of the atmosphere extending well into the thermosphere. Their primary influences at large scales depend on energy and momentum transports from sources at lower altitudes and deposition at higher altitudes accompanying wave-breaking dynamics and instabilities that cannot currently be described by global models. Responses to these small-scale dynamics in the stratosphere and lower mesosphere include local mean flow decelerations that extend large distances downstream, upstream, and laterally. The ability to describe these dynamics degrades rapidly with decreasing resolution, causing current global models to exhibit systematic circulation biases that significantly limit and degrade weather and climate prediction. We assess these impacts with a suite of simulations of wintertime flow over the S. Andes at horizontal resolutions from 0.5 to 8 km. Our results reveal that spatial resolution of ~2 km or better is required to adequately address these deficiencies extending into the mesosphere.

1. Introduction

Our understanding of the diversity of gravity wave (GW) sources, propagation, and influences on atmospheric structure and variability has advanced dramatically since their discovery at high altitudes ~60 yr ago (Hines, 1960; Witt, 1962). Many studies have highlighted the importance of GW energy and pseudo-momentum transport and deposition in accounting for the large-scale circulation and structure extending into the mesosphere and lower thermosphere (MLT); see, for example, Garcia and Boville (1994), Holton (1982), Lindzen (1981), and Smith et al. (2011), the reviews by Fritts and Alexander (2003) and Plougonven and Zhang (2014), and subsequent studies.

Also addressed by a broad community spanning many years were interactions and instabilities accounting for GW dissipation driving energy and pseudo-momentum flux divergence enabling these influences

Writing – review & editing: David C. Fritts, Thomas S. Lund, Valery Yudin

(e.g., Achatz, 2005, 2007; Andreassen et al., 1998, 1994; Bourgeat et al., 2013; Fritts & Rastogi, 1985; Fritts et al., 2017, 2009; Sutherland, 2013). Among the more recent results of such studies was the recognition of strong GW/mean-flow interactions yielding "self-acceleration" (SA) dynamics (Dong et al., 2020, 2021; Fritts et al., 2020, 2015; Scinocca & Sutherland, 2010). These comprise strong local body forcing and SA instabilities that drive secondary GWs (SGWs) arising at larger and smaller scales at higher altitudes, for which there is now additional modeling and observational evidence (Becker & Vadas, 2018, 2020; Dong et al., 2021; Lund et al., 2020). Importantly, the larger-scale SA dynamics drive large-scale SA generation of SGWs prior to the occurrence of GW breaking and instabilities.

The multiple contributions by GWs to atmospheric structure and variability, and the inability of past and present general circulation models (GCMs), and numerical weather prediction (NWP) and climate models to resolve these dynamics, have motivated developments of a wide diversity of GW parameterization schemes; see Ern et al. (2006) and Kim et al. (2003) for reviews of the earlier developments. Of the various GW sources at lower altitudes, mountain waves (MWs) have the major systematic influences on weather and climate, and the best-defined sources. Hence, major attention has focused on MW parameterization since the initial successes of such efforts (e.g., McFarlane, 1987; Palmer et al., 1986; Sandu et al., 2019).

More recently, increasing resolution of MW sources in GCMs and NWP models has motivated interests in assessing what can be directly resolved and what still requires parameterization, such as was done recently addressing convective GW generation by Stephan et al. (2019). Earlier studies addressed MW breaking and drag responses, and their comparisons, via resolved and/or parameterized MW dynamics in the "gray zone" at spatial scales currently unattainable by GCMs and NWP models. That by Doyle et al. (2005) found the Coupled Ocean-Atmosphere Mesoscale Prediction System model highest resolution of 1.7 km to capture the major features of a MW breaking event observed in the stratosphere over southern Greenland. A series of papers employing the UK Met Office Unified Model explored resolved and parameterized MW drag over South Georgia and New Zealand South Island terrain (with maximum resolutions of 1.5 and 2 km, respectively); see, for example, Fritts et al. (2018), Vosper (2015), and Vosper et al. (2016). These studies suggested that model resolutions of ~1.5–2 km are sufficient to approximate larger-scale MW and instability dynamics extending into the stratosphere under strong forcing conditions.

Such studies are currently impossible on global scales, however, and the consequences are GW sources that are significantly under-resolved, hence project onto resolved scales that may be ~5–10 times larger. From a large-scale perspective, recent modeling results at stratospheric and MLT altitudes are impressive and reveal important GW dynamics (Becker & Vadas, 2018; Liu et al., 2014). However, they fail to ascribe key dynamics to the correct spatial scales, especially those accounting for the major energy and pseudo-momentum fluxes (MFs) and deposition (or more accurately "retention"). The same limitations apply to satellite limb estimates of GW amplitudes and MFs in the stratosphere that necessarily are only sensitive to horizontal wavelengths, $\lambda_h \sim 200$ km and larger, hence cannot assess the much larger contributions expected at smaller λ_h based on modeling and theory for known source scales.

Our purposes in this paper are to quantify the consequences of degrading model descriptions of the diverse MW responses extending into the thermosphere accompanying decreasing resolution in the NWP and GCM gray zone. The model employed for these studies, the computational domain, initial and boundary conditions, and mesh refinement are described in Section 2. Section 3 summarizes results of the high-resolution simulations described by Fritts et al. (2021) and Lund et al. (2020). Impacts of decreasing resolution revealed in east-west and north-south cross-sections of perturbation winds and temperatures across, and in the lee of, the major terrain, following attainment of large MW amplitudes in the MLT, are explored in Section 4. Section 5 illustrates these impacts with horizontal cross-sections of perturbation winds, MFs, $<u'w'>$, and induced local mean winds, ΔU_h, for varying resolution at 50 and 70 km in the lower and middle mesosphere. Influences of varying resolution on momentum flux magnitudes and spectra are discussed in Section 6. The implications of these results in the context of global modeling and our conclusions are presented in Sections 7 and 8.

2. Model Description, Boundary and Initial Conditions, and Forcing

2.1. Model Description

Results presented here are obtained using the Complex Geometry Compressible Atmosphere Model (CGCAM) employed by Fritts et al. (2021) and Lund et al. (2020) for the initial simulations of these dynamics. CGCAM solves the nonlinear and compressible Navier-Stokes equations in three dimensions (3-D), written in strong conservation law (divergence) form:

$$\frac{\partial \rho}{\partial t} + \frac{\partial (\rho u_j)}{\partial x_j} = 0 \tag{1}$$

$$\frac{\partial (\rho u_i)}{\partial t} + \frac{\partial (\rho u_i u_j)}{\partial x_j} = -\frac{\partial p}{\partial x_i} - \rho g \delta_{i3} + \frac{\partial \sigma_{ij}}{\partial x_j} \tag{2}$$

$$\frac{\partial (\rho E)}{\partial t} + \frac{\partial \left[(\rho E + p) u_j\right]}{\partial x_j} = -\rho g u_3 + \frac{\partial (u_i \sigma_{ij})}{\partial x_j} - \frac{\partial q_j}{\partial x_j} \tag{3}$$

where σ_{ij} and q_j are the viscous stress and thermal conduction, defined as:

$$\sigma_{ij} = \mu \left[\left(\frac{\partial u_i}{\partial x_j} + \frac{\partial u_j}{\partial x_i} \right) - \frac{2}{3} \left(\frac{\partial u_k}{\partial x_k} \right) \delta_{ij} \right] \tag{4}$$

$$q_j = -\kappa \frac{\partial T}{\partial x_j} \tag{5}$$

Here μ is the sum of the molecular and turbulent viscosity, κ is the sum of the molecular and turbulent thermal conductivity, and δ_{ij} is the Kronecker delta. The molecular contributions to μ and κ depend on the temperature through Sutherland's Law (White, 1974) whereas the turbulent contributions are calculated via the dynamic Smagorinsky model, as discussed below.

Solution variables are density ρ, momentum per unit volume ρu_i, or $(\rho u, \rho v, \rho w)$, with velocity components $(u_1, u_2, u_3) = (u, v, w)$ along (x, y, z), and total energy per unit mass, $E = e + u_k u_k / 2$, where $e = c_v T$ and $u_k u_k / 2$ are the internal and kinetic energy per unit mass, c_v is the specific heat at constant volume, and T is the temperature. Equations 1–5 are discretized using a finite-volume (FV) method similar to that described by Felten and Lund (2006). The resulting scheme is globally conservative for mass, momentum, total energy, and kinetic energy. Our discretization is second order accurate in space and thus contains increasing errors at the smallest resolved scales.

Time stepping was performed via a low-storage, third-order accurate Runge-Kutta scheme with a fixed time step of $\Delta t = 1.2$ s for all cases having $\Delta x = 1 - 8$ km, but with that for $\Delta x = 1$ km decreasing to $\Delta t = 0.75$ s for times after 7.5 hr. As we have used variable resolution in space and among the suite of simulations addressed here, none of which resolve turbulence arising from MW or other GW breaking, all simulations employed the dynamic Smagorinsky subgrid-scale model (Germano et al., 1991; Moin et al., 1991) to account for unresolved turbulent motions. See Dong et al. (2020) and Lund et al. (2020) for additional CGCAM details.

2.2. Model Domain, Initial and Boundary Conditions, and Variable Resolution

As in Lund et al. (2020), the computational domain is Cartesian, extends 2,500 (2,000) km in longitude (latitude), 200 km in altitude, and is centered at 48°S, 73.5°W between the two major massifs of the Southern Andes, having peak terrain heights of ~3.4 and 3.8 km. Figure 1 reviews the domain, terrain, atmospheric structure, and initial conditions for convenience. The central, high-resolution domain (white lines) extends ~250 (750) km in longitude (latitude). Central horizontal resolutions of 0.5, 1, 2, 4, and 8 km are employed to explore their influences on the resulting flow evolutions. Horizontal resolution coarsens by 1.5% per FV cell away from the central high-resolution domain. Importantly, coarsening horizontal resolution causes phase errors that increase quadratically for our 2nd order scheme, and these cause reductions in GW vertical group velocities and delayed responses at higher altitudes (see Appendix A for further discussion.)

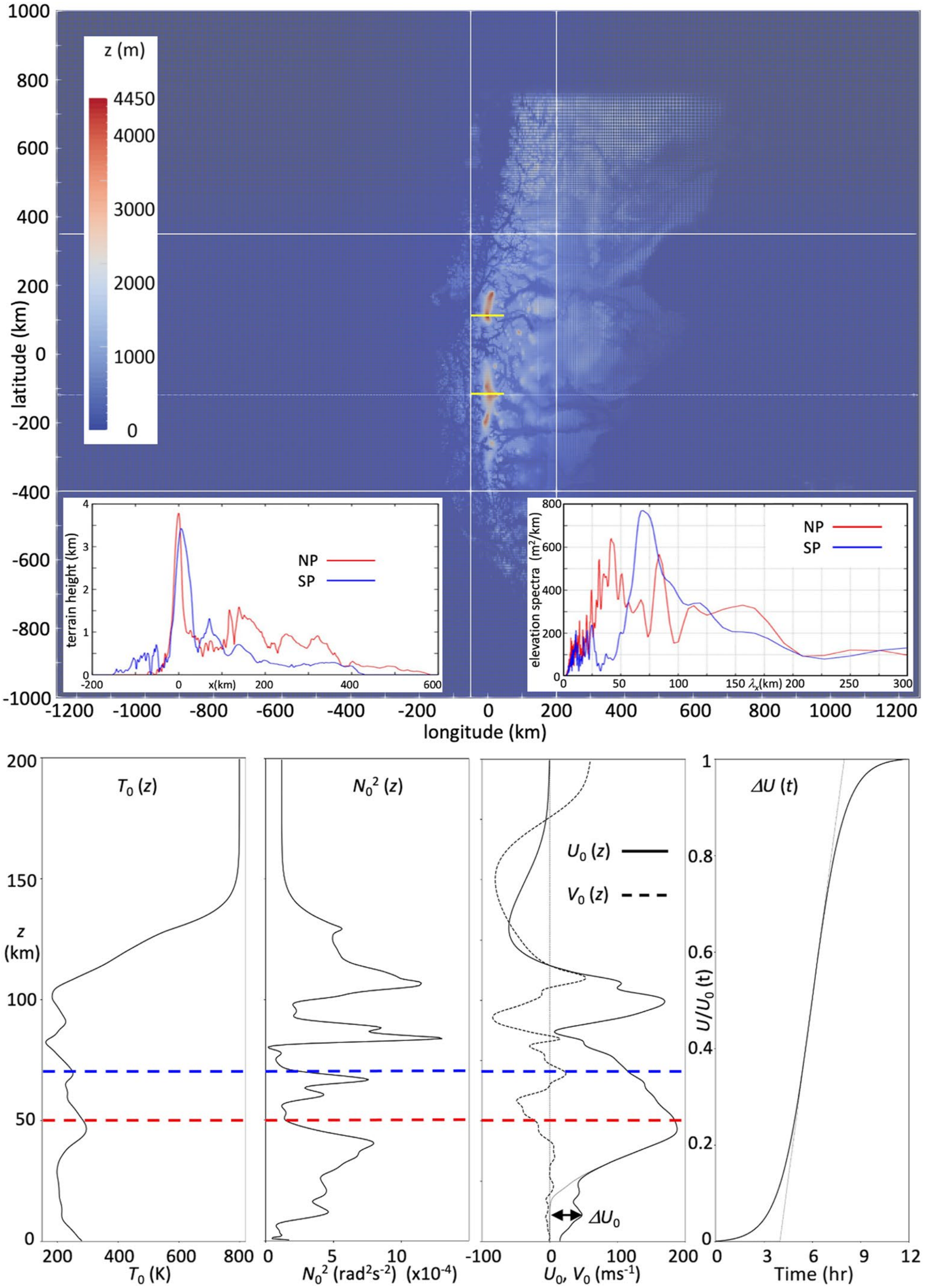

Figure 1. Complex Geometry Compressible Atmosphere Model (CGCAM) domain showing terrain height (at top). Initial profiles of T_0, N_0^2, U_0, and V_0, and the temporal ramp of ΔU are shown at bottom (left to right), with $\Delta U_0(z)$ at bottom in $U_0(z)$. Yellow lines show south peak (SP) and north peak (NP) locations. Peak NP and SP terrain heights are ~3.8 and 3.4 km; Red and blue dashed lines in the lower panels show altitudes at which x-y cross-sections are examined below.

The Southern Andes terrain was obtained from the NOAA Global Land One-km Base Elevation Project data set (Hastings et al., 1999). The terrain at the north end of the domain was artificially decreased to sea level to eliminate surface forcing near the northern boundary, making it possible to use a simple boundary condition there. The mesh at the lower boundary was distorted in order to match the terrain. These distortions were slowly reduced to zero at $z = 15$ km, yielding a purely Cartesian mesh above. East-west cross-sections over the major peaks, denoted south peak (SP) and north peak (NP), and elevation spectra over each, are shown as inset subpanels at lower left and right in the upper panel of Figure 1. The zonal wavelengths vary from $\lambda_x \sim 25$–200 km, with multiple peaks near $\lambda_x \sim 40$, 80, and ~110–170 km over NP and a single broad maximum at $\lambda_x \sim 70$ km over SP with a long tail extending to $\lambda_x \sim 180$ km.

Inflow-outflow conditions were employed at the domain boundaries in x and y, a GW radiation condition was employed at the upper boundary, and sponge layers having a *tanh*(z) depth profile of 15 km at the upper boundary and *tanh*(x or y) widths of 20 km at the lateral boundaries. The combination effectively prevented all GW and acoustic wave (AW) reflections. An inviscid (free-slip) condition was used at the lower boundary, implying neglect of the surface boundary layer, which would have required a boundary layer turbulence model and much higher resolution. A no-slip condition very slightly alters the effective terrain height and assures consistent MW forcing among our simulations having varying resolution.

2.3. Initial Conditions

Background fields are as employed by Fritts et al. (2021) and Lund et al. (2020) obtained from a free running Whole Atmosphere Community Climate Model (WACCM) simulation for July conditions. WACCM employs a spectral element dynamical core solved on a cube-sphere, with horizontal resolution of ~25 km, vertical resolution of ~0.1 scale height (H) above the middle stratosphere and higher below, and an upper boundary at 140 km. This WACCM version resolves GWs having $\lambda_x \sim 200$ km and larger. Further WACCM details are provided by Liu (2016) and Liu et al. (2014).

The wind and temperature fields at 50°S and 65°W at the time selected had a strong eastward jet at ~50 km and significant tidal influences at higher altitudes. Above 120 km, the winds were specified to approximate tidal winds asymptoting to $U_0 = 0$ and $V_0 = 70\ \mathrm{ms}^{-1}$ above 200 km to allow exploration of SGWs and AWs arising from MW dynamics at lower altitudes without constraints by large U_0 shears at higher altitudes. Initial profiles of U_0, V_0, temperature T_0, and corresponding N_0^2 are shown at bottom in Figure 1. These fields were assumed to be uniform over the domain and constant in time, as described by Lund et al. (2020), apart from departures driven by MW and other GW forcing (Fritts et al., 2021). This is because MW propagation from ~10 to 80 km occurs on short time scales due to strong zonal winds that enable the dominant MW $\lambda_x \sim 30$–80 km to have $\lambda_z \sim 15$–60 km or larger, hence to be non-hydrostatic and have large vertical group velocities, c_{gz}. Thus, the dynamics of interest occur on time scales significantly shorter than tidal periods.

To enable realistic responses having slow increases in the excitation of strong MWs, an initial $U_0(z) = 0$ to altitudes above the southern Andes peaks was assumed and ramped up to the WACCM $U_0(z)$ with a *tanh* (t/3 hr) dependence yielding 90% of its peak value at 9 hr, see the initial $U_0(z)$ shown with a thin line below 25 km) in Figure 1 (bottom, 3rd panel), and the temporal ramp in Figure 1 (bottom right). Because the initial wind and stability profiles are highly structured in altitude, the initial mean Richardson number, $Ri(z) = N_0^2/[(dU_0/dz)^2 + (dV_0/dz)^2]$, has small values, $Ri \sim 0.25$–1 from $z \sim 80$–100 km (see Lund et al., 2020), suggesting a potential for Kelvin-Helmholtz (KH) shear instabilities induced or enhanced by GW perturbations of the mean fields to also contribute to local instability dynamics, GW dissipation, and energy and momentum deposition.

3. Overview of Mountain Wave and Secondary Wave Evolutions and Dynamics

The major Southern Andes terrain in the central CGCAM domain comprises two pronounced ridges aligned largely N-S having two primary maxima denoted SP and NP by Lund et al. (2020), see yellow lines in Figure 1. The E-W terrain across SP (blue line in the inset in the upper panel at lower left) has a broader central peak and more concentrated orographic spectral responses at $\lambda_x \sim 25$ and ~50–150 km; in contrast, that across NP (red line in inset) has a narrower major peak, but significant, structured orography extending ~400 km to the east. Of these, the SP terrain yielded systematically larger MFs per unit density, $\langle u'w' \rangle$, throughout the peak responses from ~8 to 10 hr (see Fritts et al., 2021, Figure 8). Despite expected MW responses extending to $\lambda_x \sim 150$ km over SP (at $y \sim -120$ km), maximum MFs in the stratosphere and MLT were largely contributed by MWs having $\lambda_x \sim 45$–90 km. We show the stronger MW dynamics and responses with E-W cross sections over SP. N-S and horizontal cross sections at 50 and 70 km altitudes show the extensions of these dynamics over broader regions.

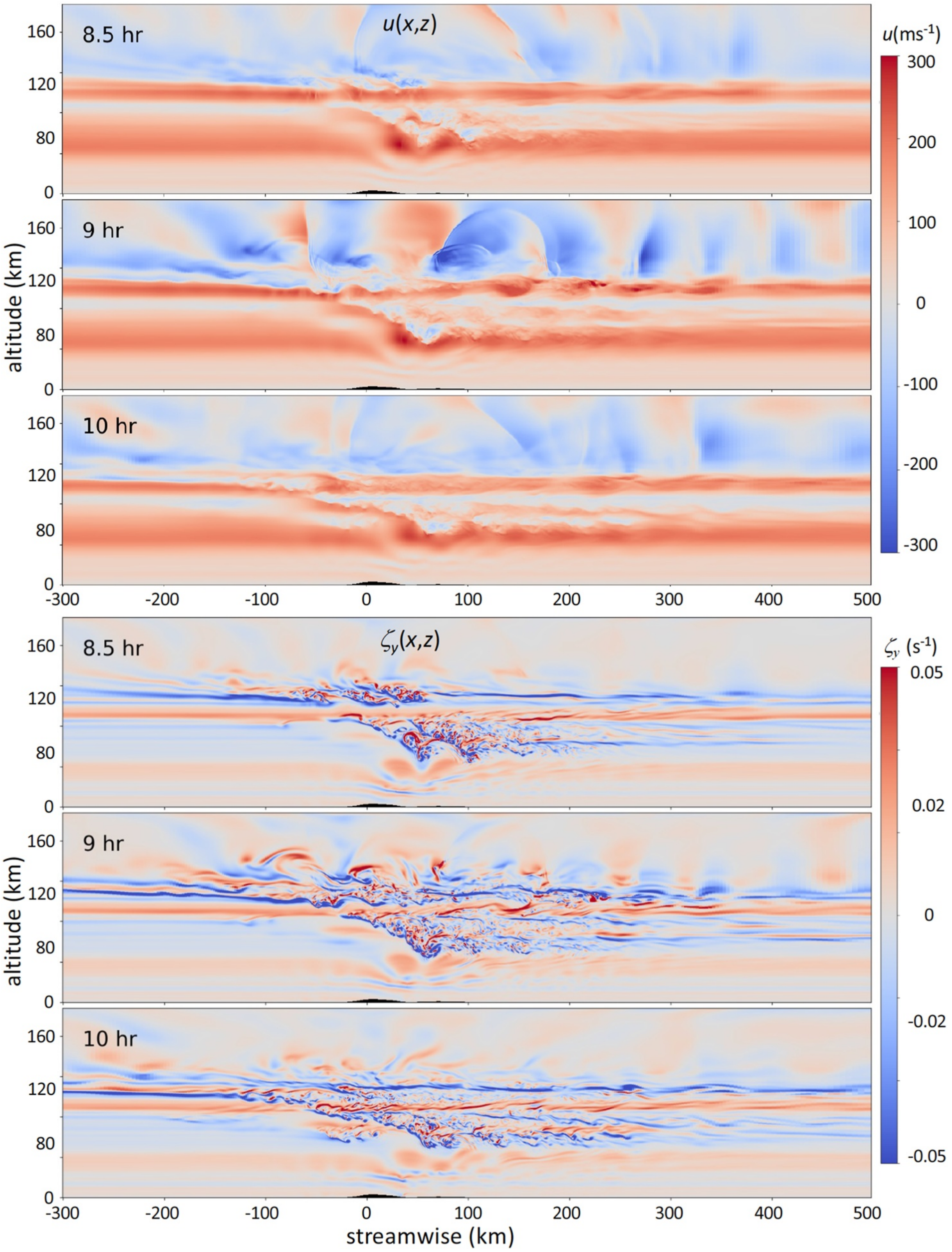

Figure 2. $u(x, z)$ and $\zeta_y(x, z)$, top and bottom panels, showing the approach to peak MW responses over SP described in detail by Lund et al. (2020).

Initial MW breaking begins at ~7.5 hr at ~70 km altitude, occurs at MW $\lambda_x \sim 45–50$ km, and expands rapidly from $x \sim 70–140$ km at ~7.5 hr to $x \sim 0–230$ km and $z \sim 65–85$ km by 8 hr (see Lund et al., 2020, Figure 6). It extends further thereafter due to the increasing MW amplitudes accompanying increasing cross-mountain flow at lower altitudes. By 8.5 hr, the region of MW breaking extends from $x \sim -100$ to 200 km, and $z \sim 45–115$ km. Breaking at higher (lower) altitudes occurs upstream (downstream) of SP; see the u' and spanwise vorticity, $\zeta_y = du/dz - dw/dx$, x-z cross-sections at 8.5 hr at top and bottom in Figure 2. The cross-sections of $\zeta_y(x, z)$ more clearly demonstrate resolution of the instabilities (i.e., vortex rings having diameters of ~5 km or larger, see Fritts et al., 2021, 2009) driving MW breaking. These also reveal MW breaking at smaller scales at $z \sim 20$ km in the lee of SP at 10 hr and thereafter accompanying attainment of peak cross-mountain flow, but these are sufficiently small to be dissipated by the LES scheme noted above.

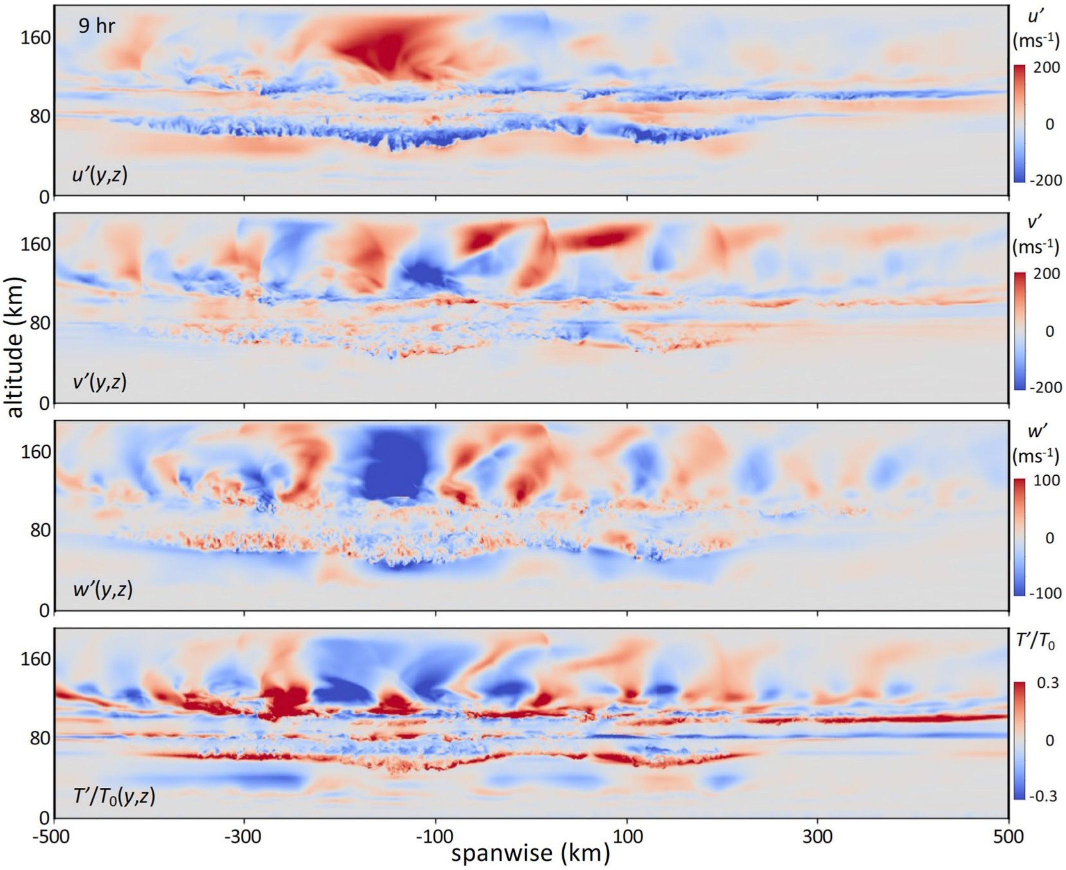

Figure 3. As in Figure 2 comparing *u'*, *v'*, *w'*, and $T'/T_0(y, z)$ at 9 hr and $x = 50$ km.

Also seen emerging at 8.5 hr in Figure 2 are SGWs occurring on smaller and larger scales. These are seen at $\lambda_x \sim 100$ km at upper left propagating upward and westward above ~115 km (a MW critical level with U and $V \sim 0$), despite $U < 0$. These must be SGWs with phase speeds $c < U$ (both negative) and intrinsic phase speeds $c_i = c - U$ increasing in magnitude where U increases at higher altitudes, consistent with λ_z increasing with altitude seen in these fields. Others are seen propagating eastward with $\lambda_x \sim 70$–100 km at $z \sim 100$ km, where they appear ducted, and above, where they are evanescent due to large, negative U.

Other responses seen primarily in u having roughly spherical phase fronts were identified by Lund et al. (2020) as AWs arising in regions of strong MW breaking at lower altitudes. These achieve $c \sim 500$ ms^{-1} and exhibit phase distortions due to the strong winds at these altitudes. They exhibit sharp phase transitions or shocks, and large, but transient, MFs having no significant influences below 200 km because they only dissipate at much higher altitudes.

MW, SGW, and AW responses in the *x-z* plane across SP continue to expand and intensify until ~9 hr, at which time the peak MW MFs occur (see Fritts et al., 2021), after which they exhibit more variable and weakening MW responses, though with a continuing large-scale flow evolution extending to later times. Corresponding *y-z* cross-sections of *u'*, *v'*, *w'*, and T'/T_0 at 9 hr and $x = 50$ km (top to bottom in Figure 3) show the comparative responses along the Southern Andes due to varying orography. These fields reveal the following features relevant to our discussion here:

1. MW breaking exhibits strong variability in altitude, with the lowest and strongest responses in the lee of the highest terrain; for example, MW breaking extends ~5–10 km lower into the upper stratosphere in the lee of SP relative to NP,
2. lower and stronger MW breaking in the lee of SP leads to significantly stronger SGW and AW generation than in the lee of NP,

3. MW breaking in the mesosphere also extends ∼1,000 km N to S over lower terrain, and
4. significant SGWs are excited that propagate over large distances N and S above ∼100 km.

Note, however, that the slow ramp of the zonal wind amplitude below ∼25 km was intended to approximate a gradual increase in cross-mountain flow enabling delayed, strong responses in the MLT, but did not enable strong MW breaking, pseudo-momentum deposition, and lower stratosphere jet decelerations during the interval discussed below.

4. Impacts of Resolution on MW and Secondary Wave Dynamics and Evolutions in Altitude

We first examine impacts of decreasing horizontal resolution (but maintaining 0.5 km vertical resolution) on CGCAM representations of MWs, SGWs, and AWs from 8 to 12 hr over which emerging MW breaking in the lower stratosphere increasingly restricts MW amplitudes entering the MLT. For these purposes, x-z cross-sections of u', w', and T'/T_0 at 8, 9, 10, and 12 hr are shown in Figures 4–6 and y-z cross-sections of u' and T'/T_0 at 9 and 12 hr are shown in Figure 7.

4.1. x-z Cross-Sections of u', w', and T'/T_0

Figure 4 showing $u'(x, z)$ over SP from 8 to 12 hr for variable Δx reveals dramatic differences in responses from the emerging (8 hr) to the decaying (12 hr) stages of MW, SGW, and AW fields. At all times, MW peak u' responses at $z \sim 40$–115 km are very similar in the central breaking region from $x \sim 0$–100 km for $\Delta x \sim 500$ m to 2 km. However, they are increasingly restricted downstream, upstream, and at altitudes above ∼80 km with increasing Δx, having qualitative similarities, but quantitative differences in amplitudes, resolution of breaking, and λ_x of the primary responses.

MW responses seen in Figure 4 degrade significantly with coarser resolution. The $u'(x, z)$ fields at $\Delta x = 4$ km begin to approximate the MW responses below ∼80 km by 9 hr, but fail to do so at higher altitudes. Those at $\Delta x = 8$ km are dramatically weaker (see the different color scales at right) and fail to approximate the high-resolution fields at all altitudes and times.

Similar impacts of varying resolution are seen in the SGW and AW responses above ∼115 km to MW breaking at lower altitudes. The $u'(x, z)$ fields at 8 hr in Figure 4 reveal earlier and stronger generation of both components due to better-resolved initial MW breaking in the mesosphere. SGW amplitudes during the peak responses from 9 to 10 hr are less impacted by model resolution because their sources are primarily local body forcing. AWs are more sensitive to model resolution because they arise due to resolved MW breaking dynamics and small-scale velocity variances, hence their responses decrease strongly as Δx increases from 0.5 to 2 km. SGWs are much weaker in the u' fields for $\Delta x = 4$ and 8 km up to 9 hr, but their relative contributions increase somewhat thereafter. Weaker SGWs at reasonable scales are seen for $\Delta x = 4$ km due to weaker, laminar MW dynamics at lower altitudes. Both primary MWs and SGWs achieve somewhat larger amplitudes for $\Delta x = 8$ km at 10–12 hr, but these occur at unrealistically larger scales (by ∼2–3 times).

The delayed and weaker responses at $\Delta x = 4$ and 8 km, and to a lesser degree at $\Delta x = 2$ km, have both physical and numerical causes. Larger Δx increasingly fail to capture the true MW and instability scales, which is physical, but they also exhibit increasing phase errors with increasing Δx, which accompany any finite-difference or finite volume scheme, and is numerical. Where features are well resolved and the initial flow transience has lessened, results for coarser resolutions converge toward results for finer resolution at earlier times. Where features are not resolved, however, coarser resolutions fail to approximate the true dynamics, as will be seen more clearly below.

Figure 5 shows corresponding $w'(x, z)$ cross-sections that highlight different features of the responses than seen in u' in Figure 4. Specifically, multiple features having smaller λ_h are not seen as clearly with the larger u' color scales. The most conspicuous are small-scale w' accompanying MW breaking and instability dynamics, especially for $\Delta x = 0.5$ km, but also for $\Delta x = 1$ and 2 km. These responses confirm the constriction of MW breaking to smaller downstream distances as resolution coarsens to $\Delta x = 1$ and 2 km, and the absence of AWs for $\Delta x = 4$ and 8 km. This is despite the w' color scales that result in clear saturation for large-amplitude AWs for $\Delta x = 0.5$–2 km at all times shown. These also show more clearly (a) ducted SGW responses from $z \sim 60$–110 km seen up to

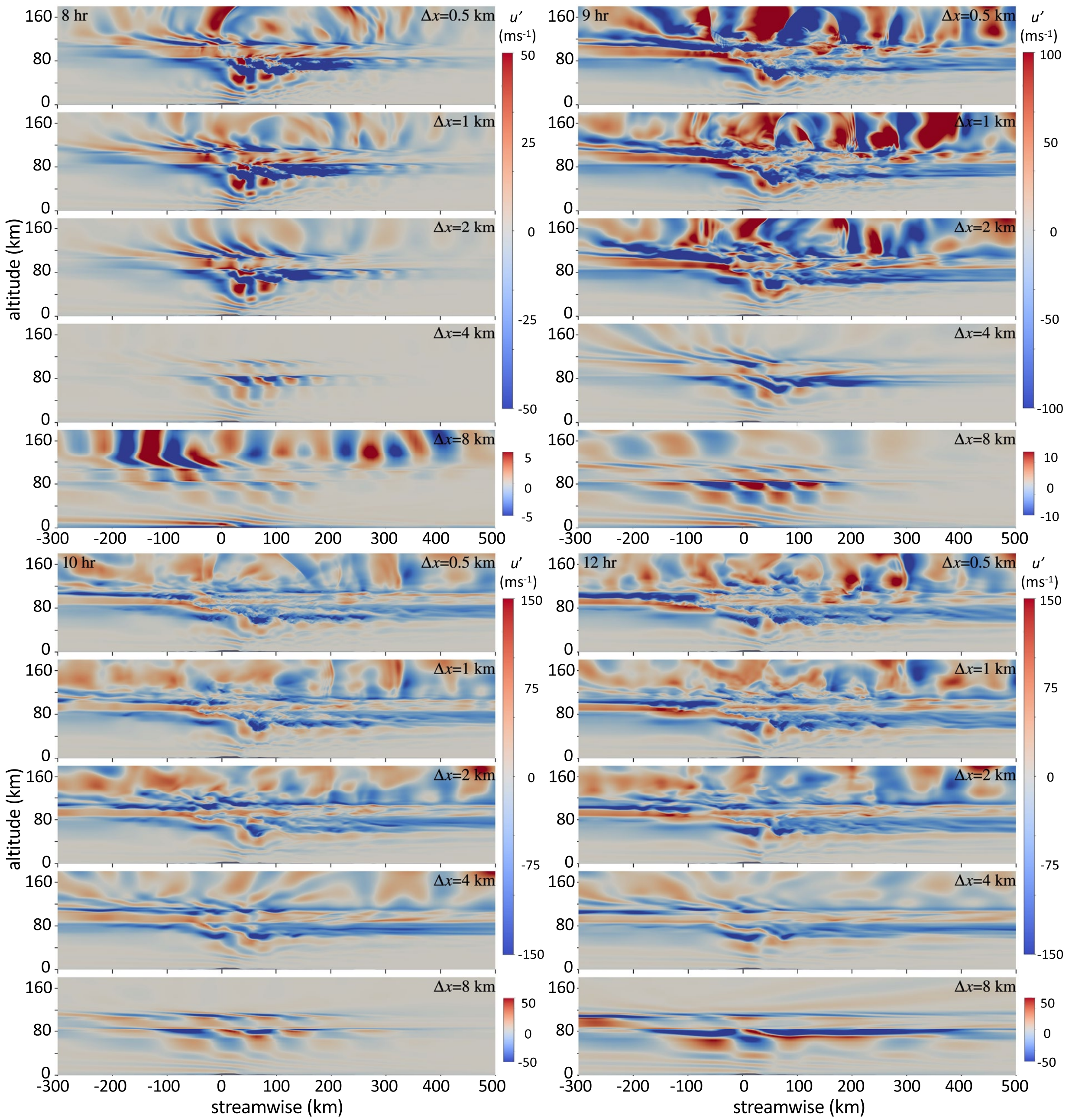

Figure 4. As in the upper panels of Figure 2, but comparing the $u'(x, z)$ responses for Δx from 0.5 to 8 km (top to bottom in each panel set) at 8, 9, 10, and 12 hr. Note the increasing color scale ranges from 8 to 9 hr, the much weaker ranges for $\Delta x = 8$ km, and the dramatic changes in the response character as resolution decreases. The color scale limits are driven by the large SGW and AW amplitudes above 100 km arising from MW breaking at ∼50–80 km.

9 hr and (b) emergence of small-scale instability dynamics at $z \sim 20$ km from ∼9 to 10 hr that likely contribute to increasing SGW amplitudes thereafter. The w' fields for $\Delta x = 4$ km confirm the emergence and λ_h of SGWs at higher altitudes from ∼10 to 12 hr seen in Figure 4. Those for $\Delta x = 8$ km (a) confirm weak MW responses at artificially large λ_h at lower altitudes, (b) reveal weak, transient SGWs at high altitudes exhibiting very large λ_h by 9 hr, and (c) exhibit no SGW responses after 9 hr, despite the very small color scale range. The w' fields also confirm the delayed responses for Δx increasing from 1 to 2 km from 9 to 12 hr and the failure of the responses for $\Delta x = 4$ and 8 km to capture true amplitudes and dominant spatial scales even at late times.

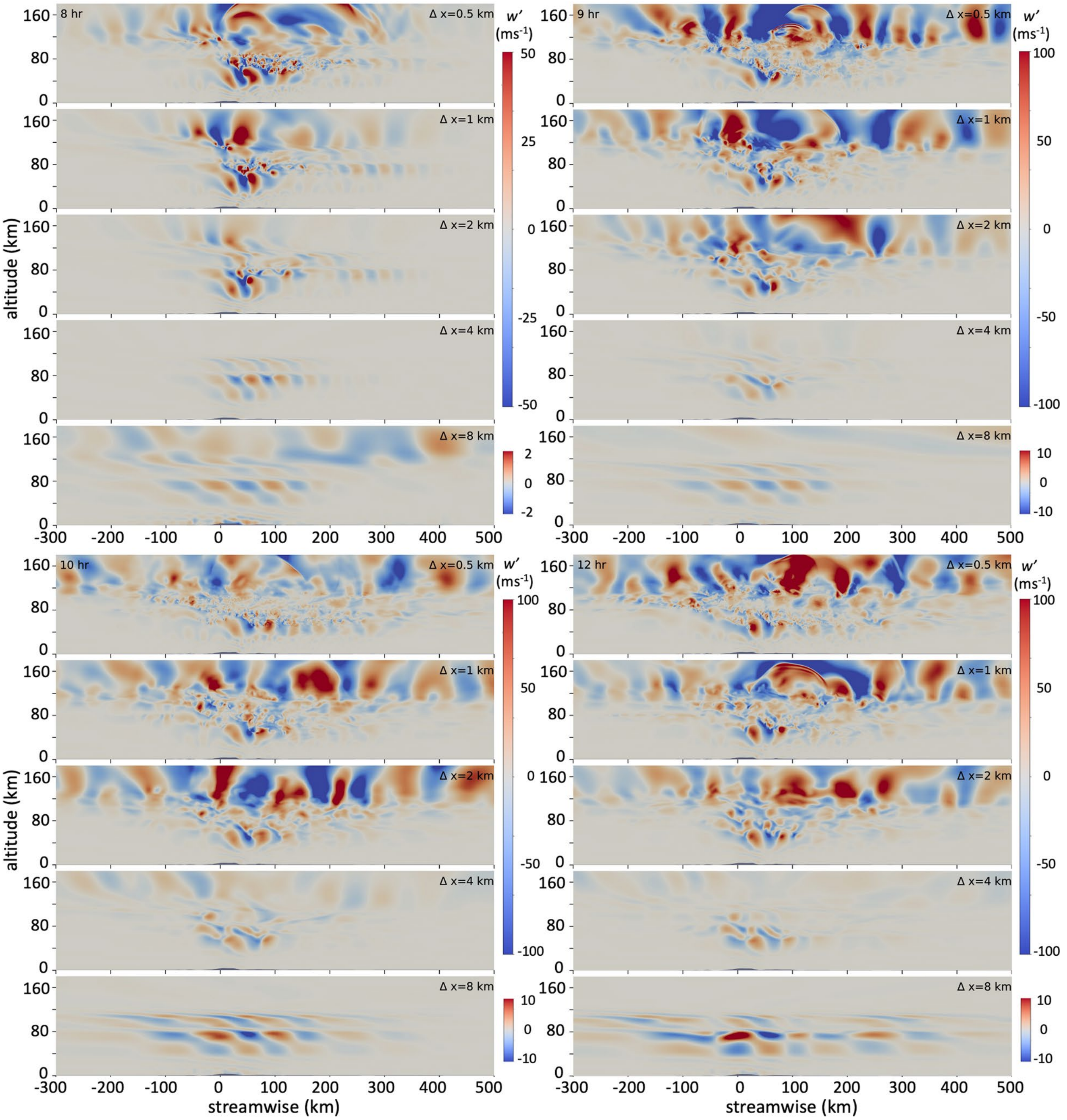

Figure 5. As in Figure 4 for $w'(x, z)$ obtained with resolution of $\Delta x = 0.5$–8 km, top to bottom. Note the significant MW responses in the stratosphere where their λ_z are very large, the larger SGWs and AWs in the thermosphere arising due to strong MW breaking at lower altitudes, and their decreasing responses for coarser resolution.

$T'/T_0(x, z)$ cross-sections shown in Figure 6 at the same times reveal more clearly some of the features noted in the u' fields in Figure 4 because u' includes sometimes significant induced mean motions. Specific features shown most clearly in T'/T_0 for $\Delta x = 0.5$, 1, and 2 km include (a) horizontal phase variations of the MW response in the lee of SP throughout the evolution, (b) shallow phase slopes of lower-frequency MWs propagating upstream above ~80 km, especially at 9 hr and after, (c) trapped SGWs propagating eastward in strong thermal ducts at ~80 and 110 km, and (d) clear positive correlations of T'/T_0 and w' due to strong AW fronts and sudden phase transitions indicating shock waves. The T'/T_0 fields for $\Delta x = 4$ and 8 km provide additional evidence of the inability of these coarse horizontal resolutions to capture any of the significant aspects of the high-resolution features of these dynamics.

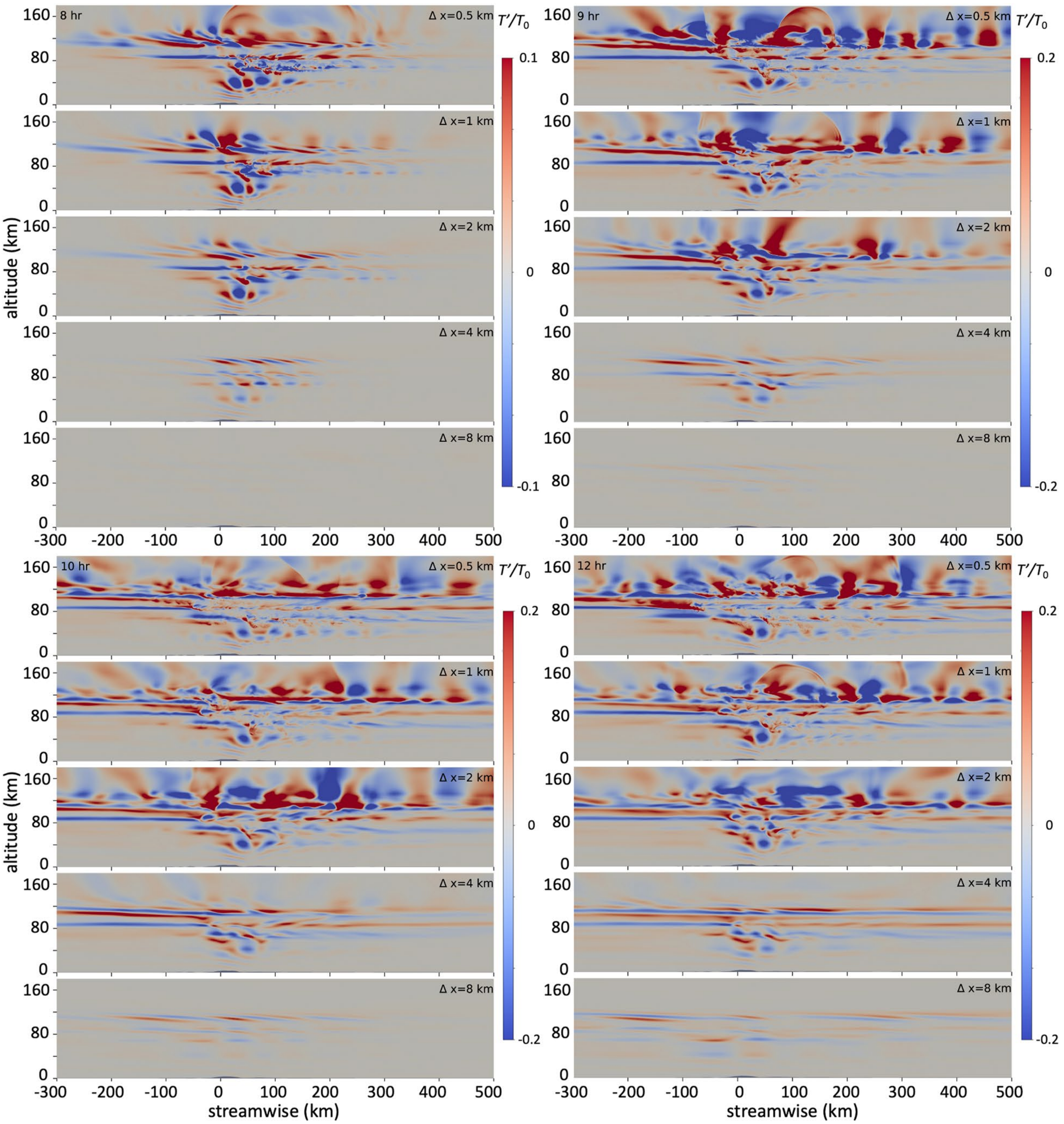

Figure 6. As in Figures 4 and 5 for $T'/T_0(x, z)$. Note the sharp transitions at the AW phase fronts for the highest resolutions and their disappearance as resolution coarsens.

4.2. *y-z* Cross-Sections of *u'* and T'/T_0

Meridional cross-sections, $u'(y, z)$ and $T'/T_0(y, z)$ at $x = 50$ km, extending over the central 800 km of those shown in Figure 3 are shown at top and bottom in Figure 7 at 9 and 12 hr (left and right). The fields for Δx = 0.5–8 km are shown from top to bottom in each panel. As noted above, *x*-*z* cross-sections over SP are broadly representative of those over NP, though with MW breaking confined to somewhat higher altitudes due to less intense forcing over more distributed lee terrain. Similar responses arise between, and north and south of, SP and NP and exhibit the layering in altitude occurring in response to the variable $U(z)$ in the MLT.

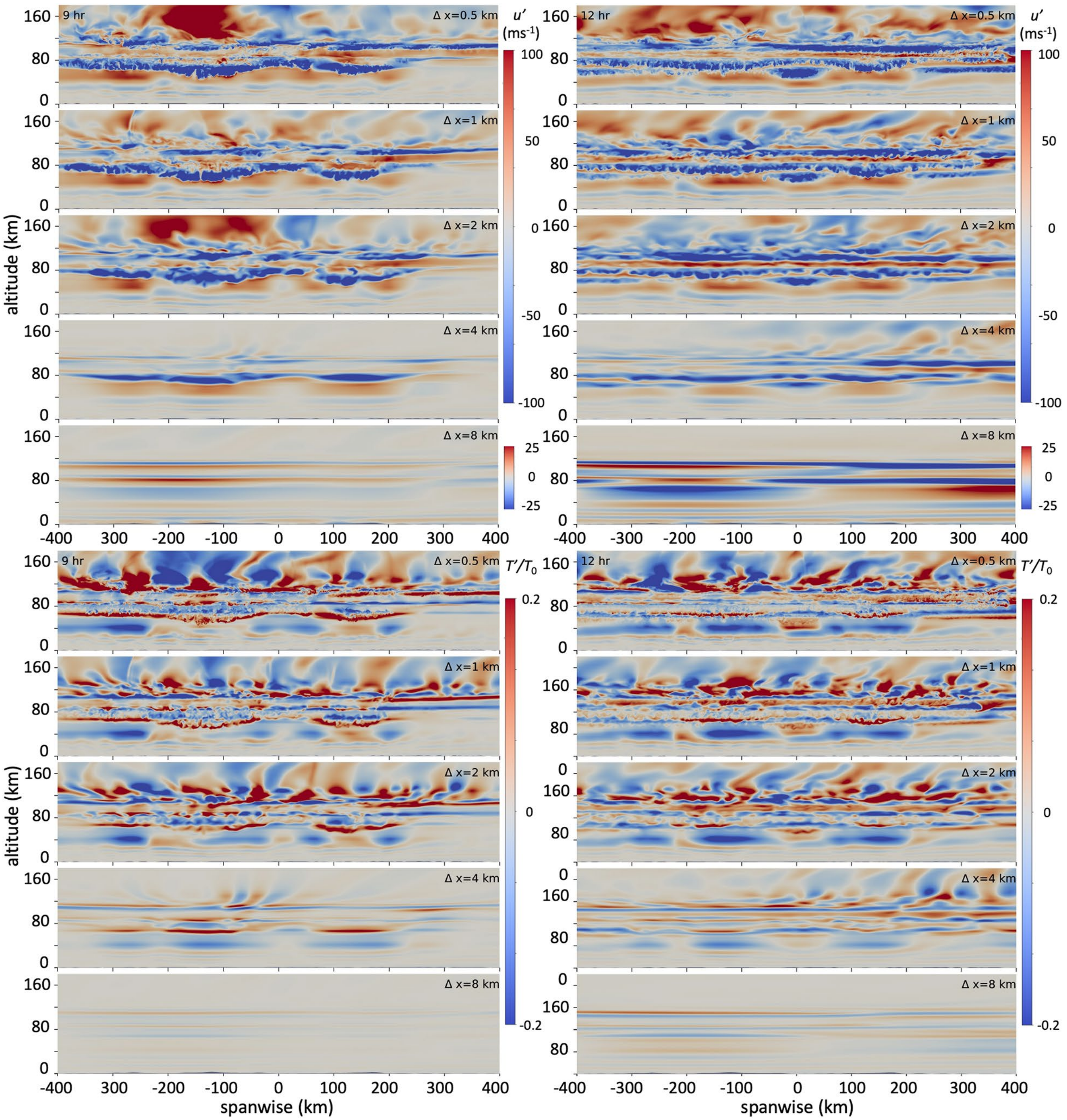

Figure 7. As in Figures 4–6 showing y-z cross-sections at $x = 50$ km of $u'(y, z)$ and $T'/T_0(y, z)$, top and bottom, at 9 and 12 hr, left and right.

Evidence of MW breaking between ~40 km and the MW critical level at ~115 km is seen in Figure 7 at 9 hr (upper left) in regions exhibiting small-scale instabilities comprising initial vortex rings revealed as "scalloped" structures (see Fritts et al., 2017, 2009) arising due to large $u' < 0$ yielding overturning with upstream $|u'| > U$, especially over SP and extending to the south. The regions of MW breaking are more extensive following the peak responses at 12 hr (upper right), where they extend continuously along the S. Andes at multiple altitudes above ~60 km. Evidence of MW breaking and instabilities is even more pronounced in the $T'/T_0(y, z)$ fields at bottom at both times because (a) these perturbations are not masked by larger induced mean fields contributing to $u'(y, z)$ and (b) they provide higher sensitivity to instability structures that are initially aligned primarily along x. Similar sensitivity to small-scale instability dynamics is also seen in $w'(y, z)$, not shown.

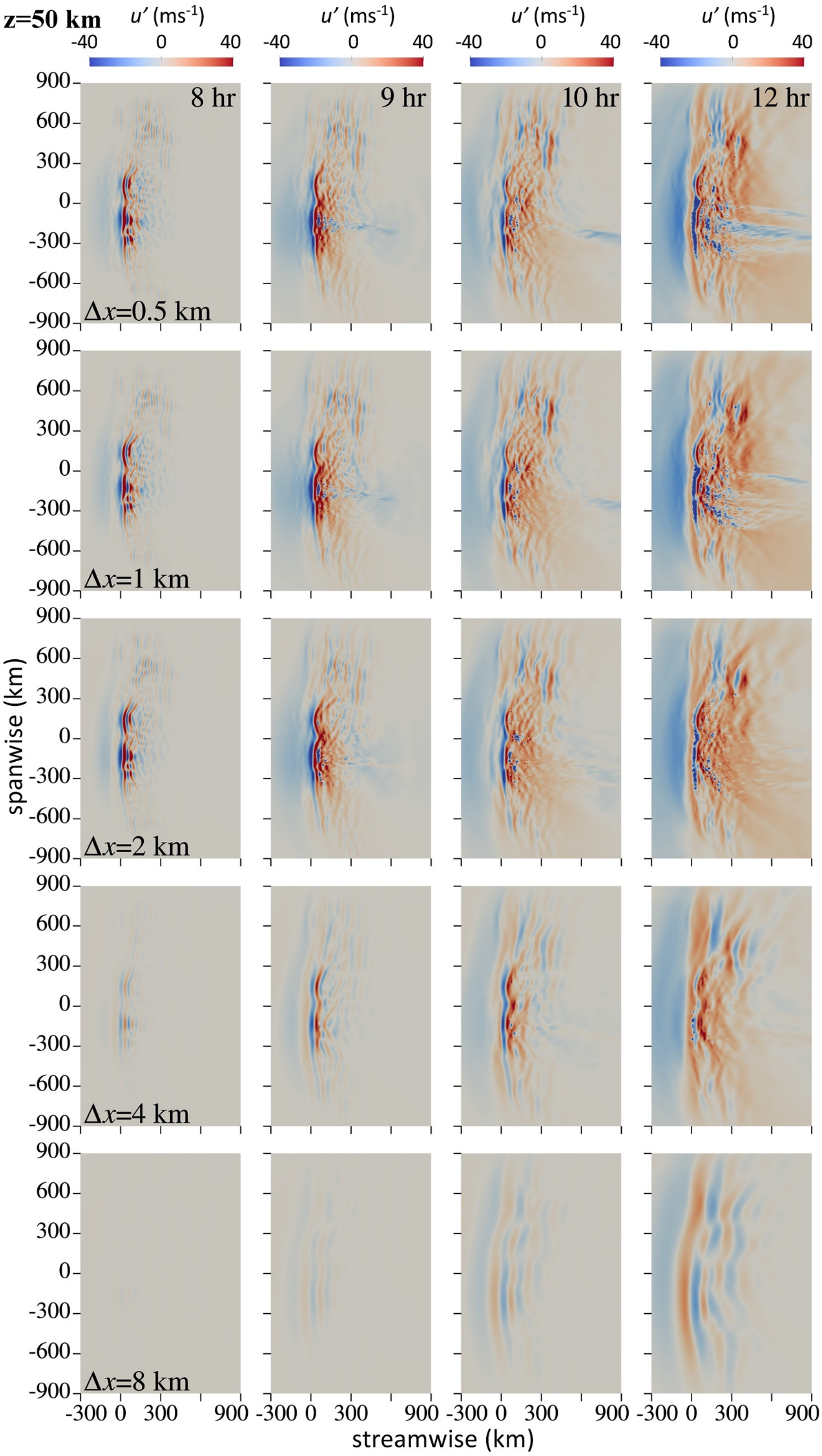

Figure 8. Horizontal cross-sections of $u'(x, y)$ at $z = 50$ km (red dashed lines at bottom in Figure 1) and 8, 9, 10, and 12 hr, right to left, for $\Delta x = 0.5$–8 km, top to bottom.

Comparing small-scale structures revealed in the $u'(y, z)$ and $T'/T_0(y, z)$ fields in Figure 7 for $\Delta x = 0.5$, 1, and 2 km, we see that each successive reduction in resolution removes features that are present at the higher resolution. This is because the finest-scale instability dynamics arising at $z \sim 45$–50 km have spatial scales as small as

~3 km (yielding initial vortex rings having diameters as small as ~5 km). In order to have confidence in these assessments, we also performed a test simulation in a very small domain with isotropic $\Delta x = 250$ m that yielded comparable instability scales, thus providing confidence in the 500-m resolution results discussed here. We note, however, that GW instability scales are, in general, constrained by the GW parameters, primarily λ_z and c_i, and that large-scale vortex rings require large λ_z and c_i (Fritts et al., 2017, 2009).

Despite differing resolved instability dynamics for $\Delta x = 0.5$, 1, and 2 km, the $u'(y, z)$ and $T'/T_0(y, z)$ fields exhibit very similar large-scale responses at breaking altitudes because they all effectively limit MW amplitudes, though via the LES scheme at coarser resolution, and account for momentum deposition driving these responses. The differing resolutions do have some impacts on SGWs and AWs seen at higher altitudes because their forcing dynamics become less efficient at coarser resolution.

The y-z cross-sections for $\Delta x = 4$ km, in contrast, approximate the larger-scale responses where MW λ_z and c_i are large at ~40–70 km, but degrade strongly at higher altitudes. Those for $\Delta x = 8$ km capture no realistic features, badly mis-represent the MW responses, and exhibit no SGWs.

5. Impacts of Resolution on MW Evolutions, MFs, and Mean Responses in the Mesosphere

We now examine impacts of decreasing resolution on MWs and induced local-mean flows, $<\Delta U>$, in the lower and middle mesosphere. These are shown at 9–12 hr with $u'(x, y)$ at 50 and 70 km and $v'(x, y)$ at 70 km in Figures 8–10, $<u'w'>(x, y)$ in Figure 11, and $<\Delta U>(x, y)$ in Figures 12 and 13.

5.1. x-y Cross-Sections of u' and v'

Cross-sections of $u'(x, y)$ and $v'(x, y)$ in Figures 8–10 correspond approximately to the altitudes of peak $<u'w'>$ in the lee of SP and NP discussed by Fritts et al. (2021). Those for $v'(x, y)$ in Figure 10 are shown only at 70 km where initial MW responses are smaller, but induced decelerations are comparable or larger and more extended along the Southern Andes, and spanwise variations of initial zonal decelerations yield significant, emerging $v'(x, y)$.

The $u'(x, y)$ fields at 50 km in Figure 8 reveal a number of features and inferred dynamical contributions that vary strongly with resolution and time. Evidence of these MW influences includes (a) bowing of MW phases westward over, and in the lee of, NP and SP relative to other sites and (b) vertical undulations of the MW breaking zones in altitude along y seen in Figures 3 and 7 due to their westward displacements. All cases yield the largest MW amplitudes over and in the immediate lee of NP and SP, but these responses are successively weaker for $\Delta x = 1$ and 2 km, much weaker for $\Delta x = 4$ km, and absent or confined to larger λ_x and later times for $\Delta x = 8$ km. Larger MW λ_x extend increasing distances downstream and upstream at later times for all resolutions due to (a) contributions of downstream orography (see Figure 1) and (b) their smaller and shallower group velocities. MWs having the smallest λ_x able to avoid evanescence contribute the major pseudo-momentum and energy fluxes into the stratosphere and mesosphere, but these are poorly or unresolved, respectively, for $\Delta x = 4$ and 8 km. Larger pseudo-momentum fluxes in the lee of NP and SP account for strong, sustained zonal flow decelerations (see the $u' < 0$ wakes) prior to MW breaking and pseudo-momentum deposition for $\Delta x = 0.5$ km, but which decrease significantly for $\Delta x = 1$ km, and are not apparent for larger Δx.

These various responses are driven by small-scale MW breaking and instability dynamics yielding pseudo-momentum flux divergence and local-mean forcing that likewise exhibit significant reductions in intensities (and resulting flux divergence) for increasing Δx. As noted above, these instability dynamics comprise primarily vortex rings having ~3–5 km diameters that are reasonably approximated for $\Delta x = 0.5$ km, but which are poorly described or unresolved for larger Δx. MW dissipation and pseudo-momentum deposition also occur at smaller MW λ_z, but in these cases, MW dissipation is driven entirely by the subgrid-scale model.

The most pronounced differences of $u'(x, y)$ at 70 km (Figure 9) relative to those at 50 km are the emergence of strong wakes of increasing and expanding negative u' with time. Reference to Figure 4 reveals that MW $\lambda_x \sim$ 100 km and larger modulate the wakes weakly, but cannot account for their large negative u' expanding to over ~1,000 km along x and y at later times. Rather, the wakes arise due to cumulative pseudo-momentum deposition

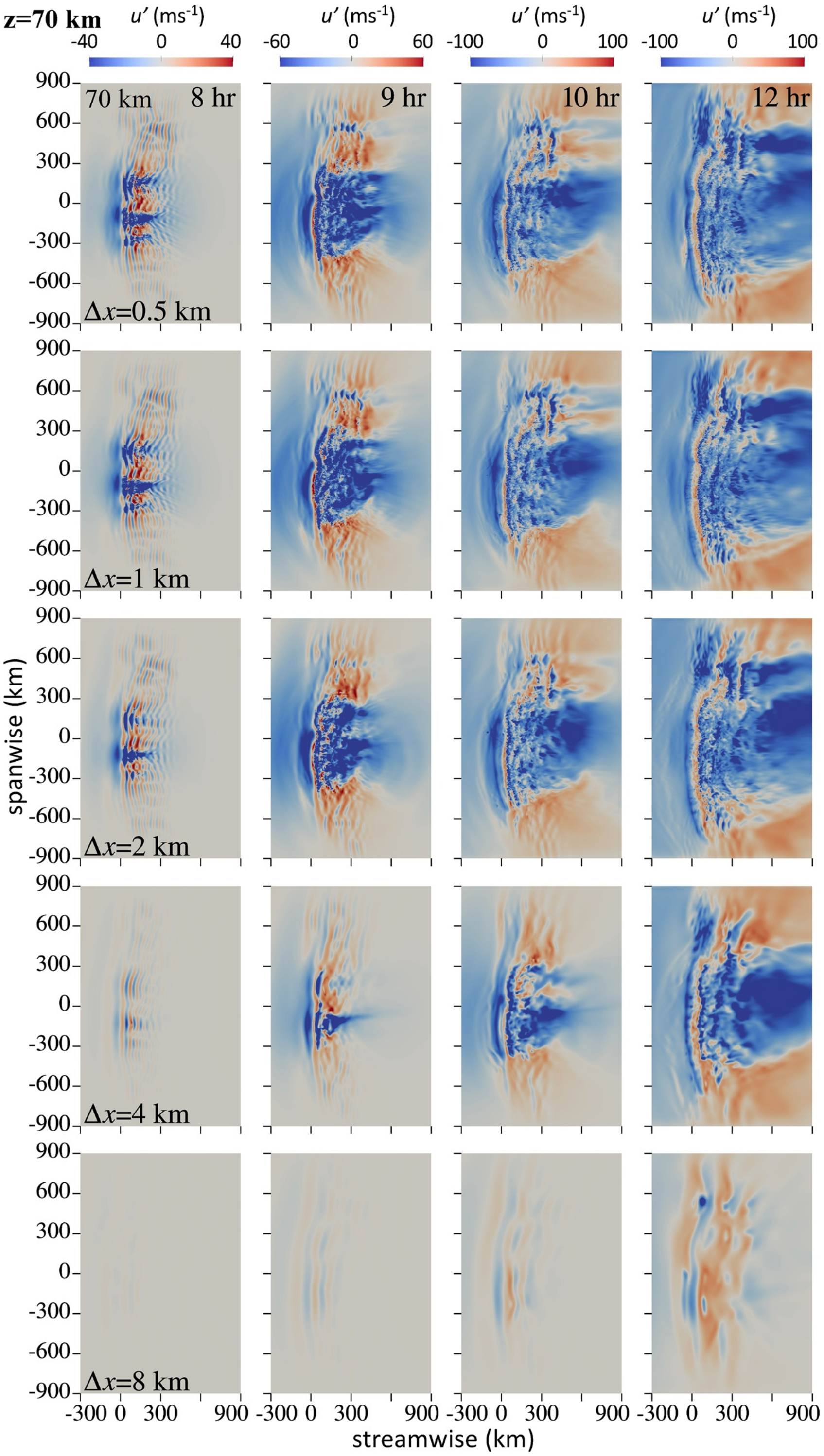

Figure 9. As in Figure 8 for $u'(x, y)$ at 70 km (blue dashed lines in Figure 1).

and their advection downstream (toward larger x) thereafter. The dynamics are the same as described at 50 km and by Fritts et al. (2021), but are much stronger and more extended along y at 70 km. This is because MW breaking only occurs at 50 km from $y \sim 0$ to ~300 km southward at later times whereas it expands from ~600 km along y at 9 hr to ~1,200 km at 12 hr. More significantly, induced decelerations seen in Figures 8 and 9 in the lee of the

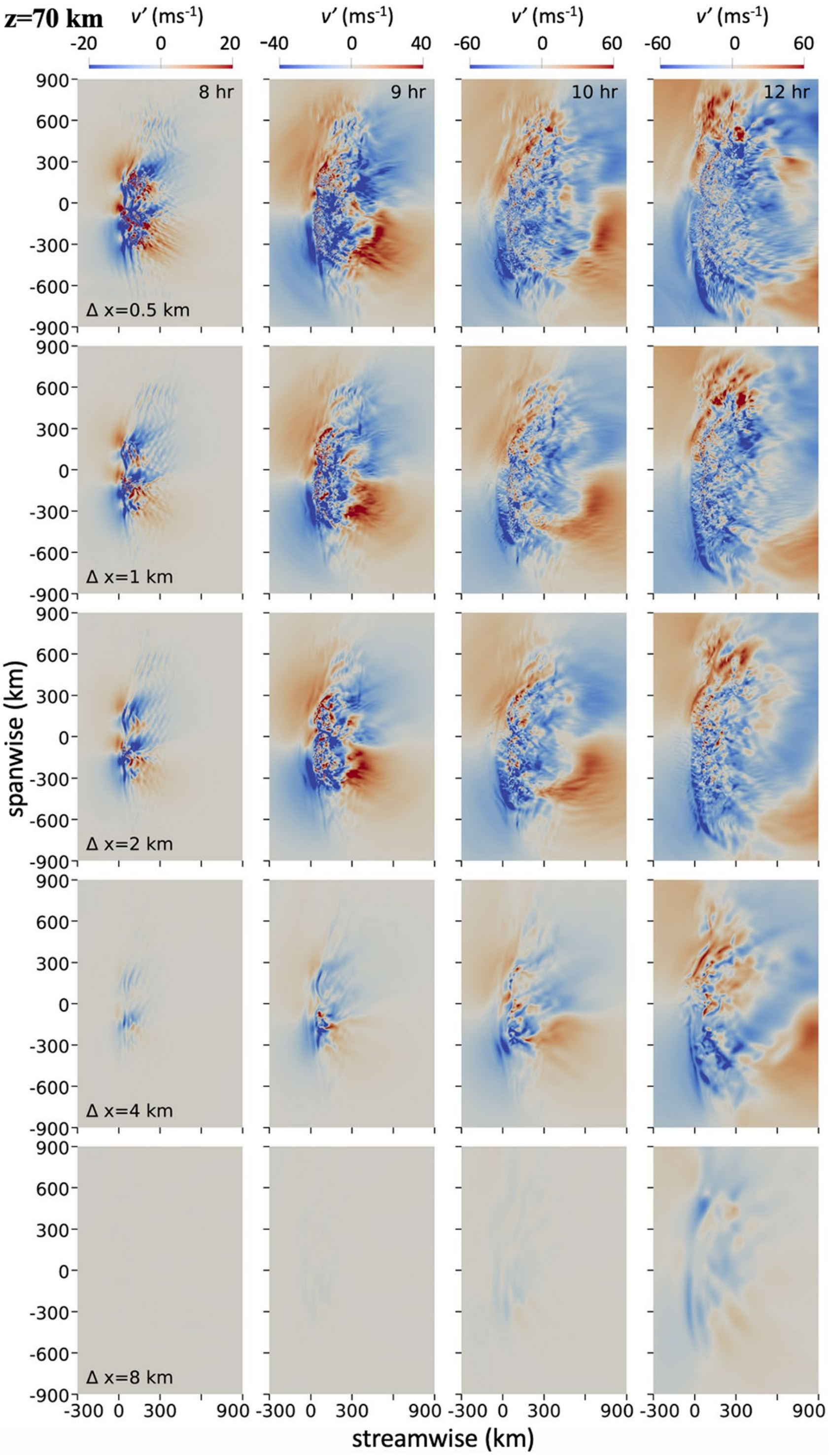

Figure 10. As in Figure 9 for $v'(x, y)$ at 70 km.

Southern Andes vary as $dU/dt \sim \langle u'w'\rangle/H$, assuming MW breaking yields time-mean $\langle u'w'\rangle$ varying much more slowly than ρ in altitude. Cumulative effects as these responses are swept downstream through extended regions of MW breaking along x yield weak, spanwise-localized mean $u' < 0$ "wakes" at 50 km in the lee of the major Southern Andes peaks that diminish rapidly with increasing Δx.

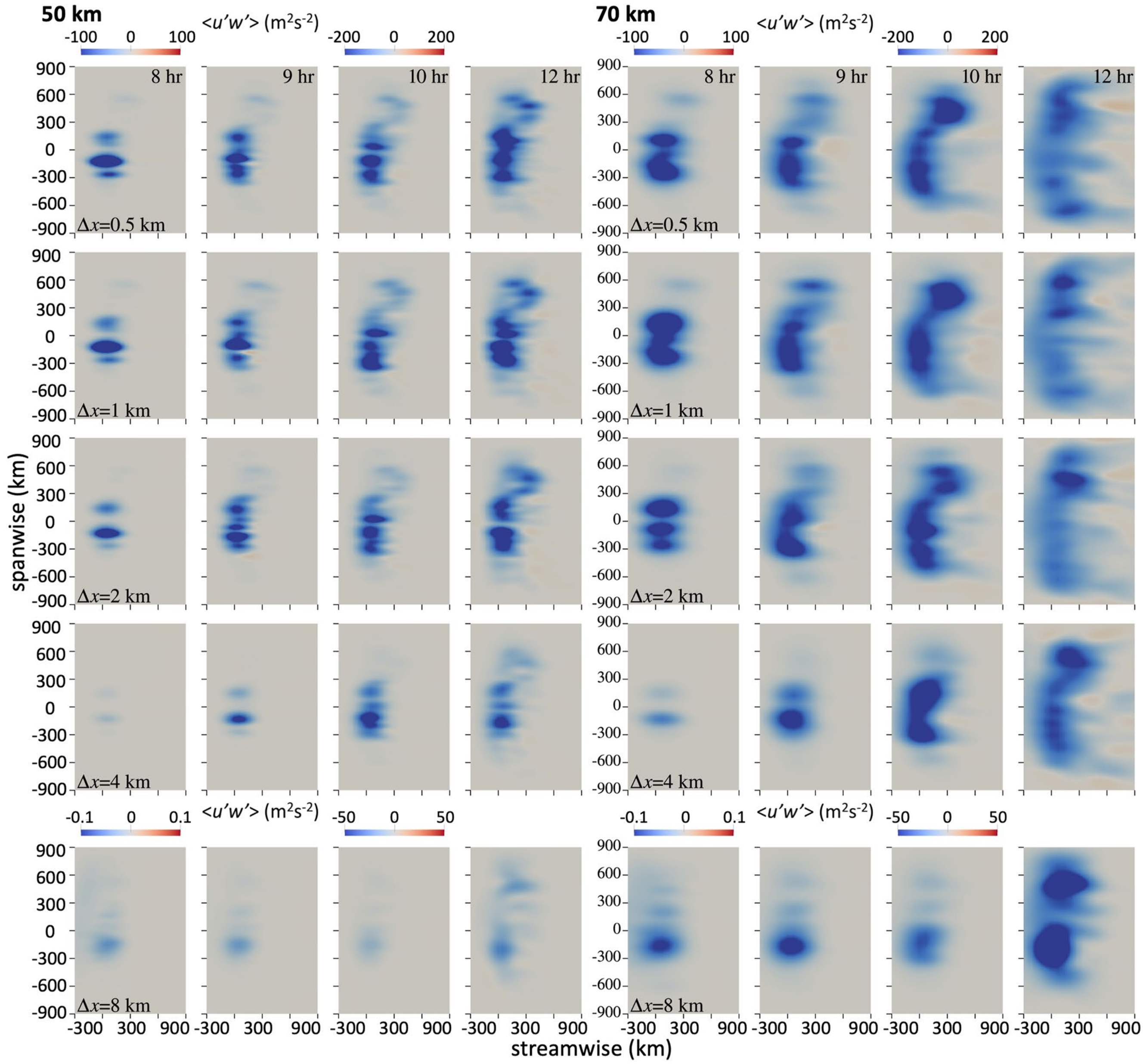

Figure 11. MW $<u'w'>(x, y)$ averaged as described in the text at 50 and 70 km at left and right, respectively. Note that the color scales are saturated at various times and locations.

These dynamics yield dramatically stronger and more extensive MW responses at 70 km due to widespread breaking and dU/dt varying as $1/\rho$ (thus a factor of ~20 larger at 70 km relative to 50 km) for comparable peak time-mean $<u'w'>$. Significant $u' < 0$ wakes emerge by 8 hr in the lee of NP, from SP southward to $y \sim -200$ km, and more weakly at $y \sim -300$ km for $\Delta x = 0.5$ and 1 km. These regions intensify, expand, and merge along y by 9 hr, and have large-scale features that agree closely for $\Delta x = 0.5$–2 km to 12 hr. Similar responses, but further delayed in time and differing in lee response details, are also seen for $\Delta x = 4$ km. Not surprisingly, given discussions above, responses for $\Delta x = 8$ km exhibit no similarities to those for $\Delta x = 0.5$–4 km at any time.

Specific differences in these evolutions include the following:

1. emergence of a narrow $u' < 0$ downstream wake response at $y \sim 600$ km beginning at ~9 hr for $\Delta x = 0.5$ and 1 km, at ~10 hr for $\Delta x = 2$ km, but never appearing for $\Delta x = 4$ km,

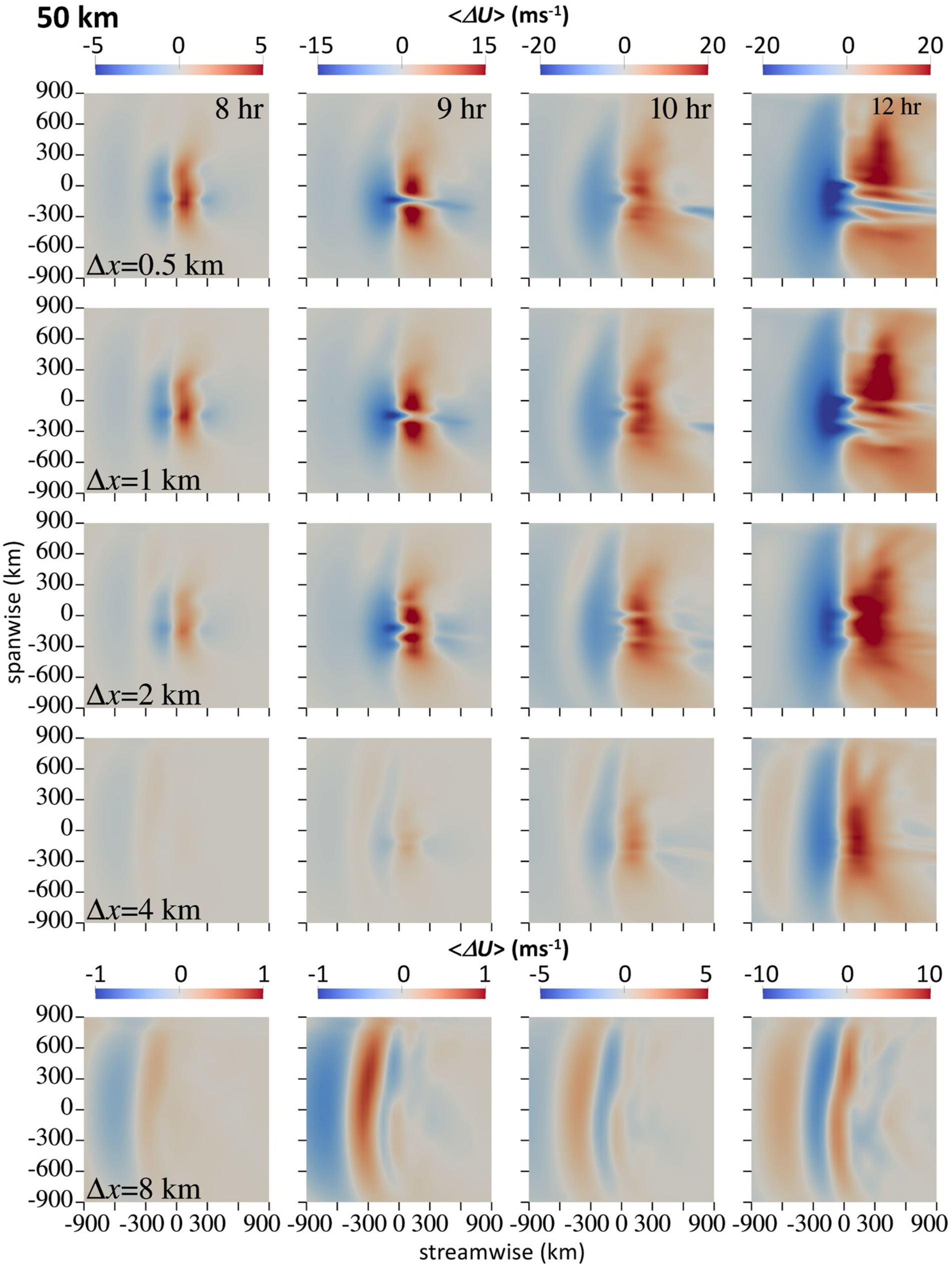

Figure 12. As in Figure 11 for <ΔU>(x, y) at 50 km averaged along x (y) over 200 (50) km. Note the larger streamwise domain to display upstream and downstream induced changes for varying Δx and time. <ΔU>(x, y) fields at 70 km in Figure 13 display the wake responses more clearly than seen in Figure 9. These confirm the intensifying and expanding wakes from the lee of the Southern Andes to over 900 km downstream and extending to over 1,000 km along y by 12 hr for Δx = 0.5–2 km. They also further quantify the weaker and delayed responses with increasing Δx.

2. emerging, strong (~50 ms^{-1} or larger) spanwise variations in downstream u' wakes having spanwise scales of ~300–500 km for Δx = 0.5 km, similar, but weaker, wakes for Δx = 1 km, and tendencies for emerging, larger-scale spanwise wakes for Δx = 2 and 4 km,
3. an emerging and expanding wake at 10–12 hr for Δx = 4 km that attains a similar u' to those for Δx = 0.5–2 km, but closely resembles the latitudinal structure for smaller Δx at 10 hr, and
4. extension of apparent MWs having λ_x ~ 50–200 km or larger upstream with increasing time, but more prominently for smaller Δx.

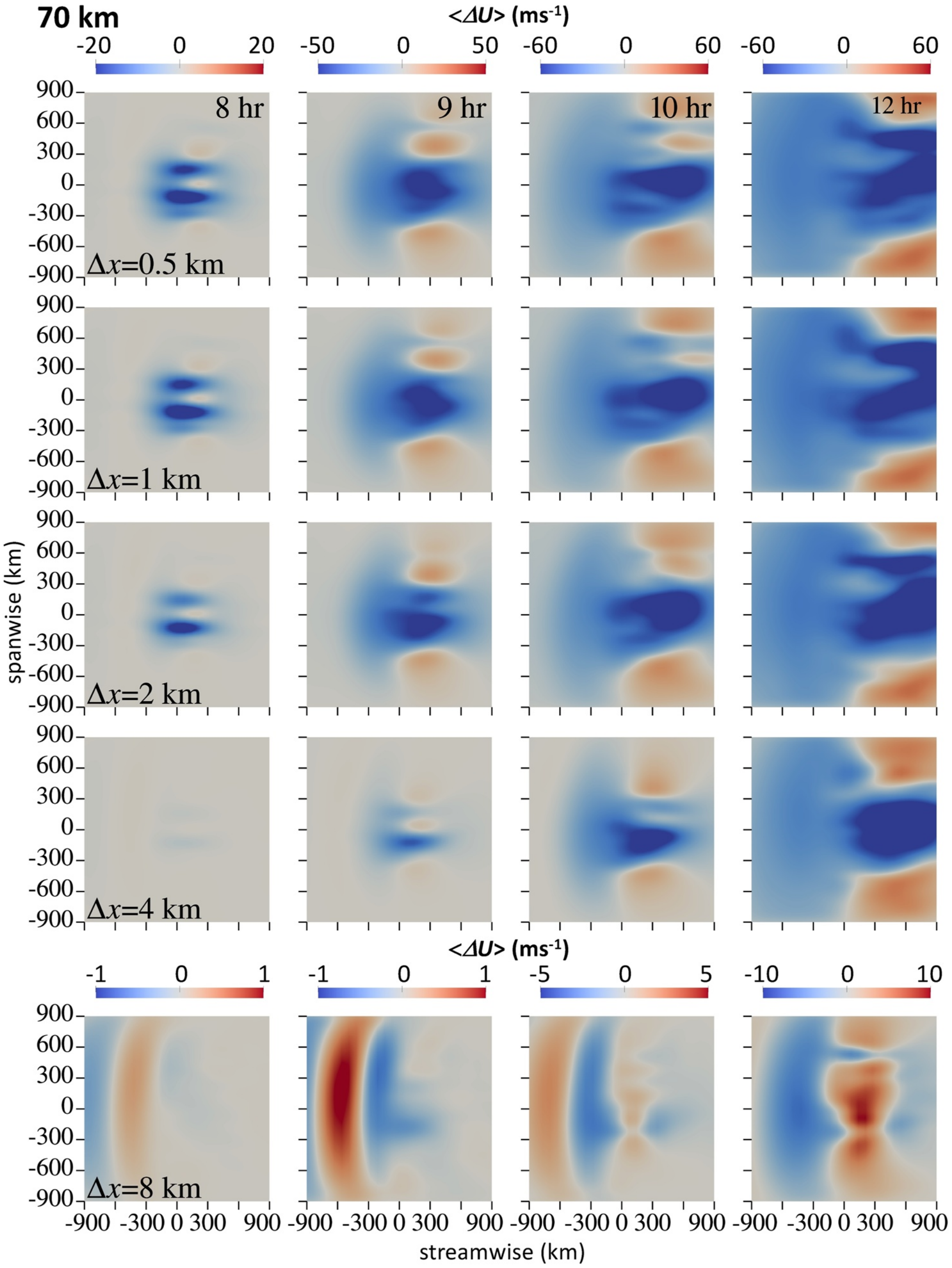

Figure 13. As in Figure 12 at 70 km averaged along x (y) over 300 (100) km.

Differential advection of MW phases along y due to spanwise variations of time-mean $<u'w'>$ and induced local-mean departures alter MW orientations and induce $v'(x, y)$ and local-mean $<v'>$ seen in Figure 10. These fields reveal (a) larger-scale responses to MW pseudo-momentum deposition and the emerging $<u'>$ over and in the lee of the major Southern Andes terrain and (b) smaller-scale features due to local responses to smaller-scale terrain within the larger field.

The large-scale responses are essentially induced horizontal vortex dipoles, with positive (negative) vertical vorticity at $y < 0$ (>0), inferred from large-scale v' arising from large-scale westward accelerations yielding $<u'> < 0$ in a confined region along x and y. This results in (a) spanwise divergence (convergence) to the west (east) of the major induced $<u'> < 0$ and (b) compensating $<u'> < 0$ at smaller and larger y. The two vortex cores for $\Delta x = 0.5$ km appear to expand spatially and advect downstream from $x \sim 150$ km at 8 hr to $x \sim 600$ km at 10 hr as MW breaking progresses eastward, with less distinct motions at large x thereafter. Their upstream edges extend westward of the Southern Andes as they arise and have persistent responses throughout the evolution.

The forms of these large-scale dipole responses are similar for $\Delta x = 1$–4 km, but their intensities and spatial extents in x and y decrease with increasing time. These decreasing responses are due to the weaker u', w', $<u'w'>$, downstream extents of MW breaking, and implied local $<\Delta U>$ in these regions for increasing Δx (see the u' and w' fields in Figures 4 and 5 spanning these times). Smaller-scale responses are smaller versions of these dipoles centered slightly downstream of the major orography in each case. The variable 3-D responses to these local pseudo-momentum depositions also yield induced, and variable, U, V, and W (x, y, z, t) that span the full extent of the MW response over, downstream, and upstream of the Southern Andes (see Fritts et al., 2021). Of the responses for $\Delta x > 0.5$ km, those for $\Delta x = 1$ and 2 km approximate that for $\Delta x = 0.5$ km, but with ~30% and 60% weaker intensities and extents. That for $\Delta x = 4$ km is dramatically smaller and weaker, but does have peak v' and local-mean $<v'>$ approaching those for smaller Δx. The response for $\Delta x = 8$ km captures no details resembling the higher-resolution results.

5.2. *x-y* Cross-Sections of $<u'w'>$ and $<\Delta U>$

Horizontal cross-sections of $<u'w'>$ and $<\Delta U>$ were averaged using Gaussian weighting having full-width, half maximum values along x (y) of 200 (50) km at $z = 50$ km and 300 (100) km at $z = 70$ km, respectively. These reveal the regions of major forcing and responses in the lower and middle mesosphere throughout the 8 to 12 hr interval discussed above. The $<u'w'>(x, y)$ fields extending to +/−900 km along y and from −300 to 900 km along x at $z = 50$ and 70 km are shown at left and right in Figure 11, respectively. Corresponding $<\Delta U>(x, y)$ at 50 and 70 km, but extending to $x = -900$ km, are shown in Figures 12 and 13.

The $<u'w'>(x, y)$ fields in Figure 11 reveal the expanding MW influences with altitude and time. They also confirm the constraints on MW amplitudes due to breaking that is highly localized at 50 km, but which is stronger and constrained by decreasing U (and $|c - U|$) at 70 km. The latter accounts for the similar peak $<u'w'>$ at the two altitudes, despite the decrease in ρ by ~20.

Peak $<u'w'>$ at all times occur over and in the immediate lee of the major Southern Andes orography. The responses extend somewhat north of NP and further south of SP due to the more extended high terrain to the south, as seen more clearly in Figures 8 and 9. Peak $<u'w'>$ remain more localized throughout the event at 50 km, but become more uniform along the major terrain where MW breaking is more continuous at 70 km. These responses also extend over larger x and y at later times as MWs having larger λ_x reach these altitudes. The maximum negative averaged magnitudes are ~400 to 600 m^2s^{-2} and ~300 m^2s^{-2} at 50 and 70 km, respectively.

As noted in the discussion of $u'(x, y)$ and $v'(x, y)$ above, the $<u'w'>(x, y)$ at 50 and 70 km exhibit close agreement for $\Delta x = 0.5$, 1, and 2 km, with weak, but discernible, differences at all times. Unlike $u'(x, y)$, however, $<u'w'>(x, y)$ exhibit maxima that are much more confined because MW $<u'w'>$ vary as u'^2/λ_x, hence are largest over and in the near lee of the Southern Andes orography. As seen in $u'(x, y)$ in Figures 8 and 9, $<u'w'>(x, y)$ for $\Delta x = 4$ km are more confined and intense over and in the lee of the major orography at all times, but do approximate those for smaller Δx at earlier times. The responses for $\Delta x = 8$ km are much weaker and bear little resemblance to those for smaller Δx at any times.

$<\Delta U>(x, y)$ fields at 50 and 70 km in Figures 12 and 13 largely confirm inferences from the $u'(x, y)$ fields. As noted above, the major responses at 50 km shown in Figure 12 largely reflect the increasing amplitudes of primary MWs having larger λ_x at later times yielding peak $<\Delta U>\sim$ 20–25 ms^{-1} from 9 to 12 hr. They nevertheless also reveal the influences of MW dynamics yielding narrow $\Delta U < 0$ wakes with magnitudes of ~15–25 ms^{-1}, despite the increasing influences of the $u' > 0$ phase of MWs having larger λ_x at this altitude. Whereas these wakes are seen clearly for $\Delta x = 0.5$ and 1 km, they disappear rapidly with increasing Δx and are absent for $\Delta x > 1$ km. The $<\Delta U>$ responses for $\Delta x = 8$ km are similar with respect to the larger λ_x responses, but are very weak and exhibit no wakes.

The strong $<\Delta U>$ wakes at 70 km are consequences of the much larger and sustained negative local $dU/dt \sim <u'w'>/H$ accompanying MW breaking relative to those seen to occur at 50 km. They extend >900 km due to continuous breaking along the Southern Andes by 12 hr (see Figure 7), and advection of the decelerated regions to large distances downstream thereafter. Peak negative $<\Delta U>$ at 10–12 hr are as large as ~100 ms^{-1} over extended regions from $x \sim$ 100–900 km and $y \sim -400$ to 600 km. As seen in Figure 12, $<\Delta U>$ for $\Delta x = 4$ km approximates those for smaller $\Delta x = 0.5$–2 km at earlier times, but those for $\Delta x = 8$ km have much smaller amplitudes and do not (Figure 14).

5.3. MW Momentum Flux Spectra Over NP and SP

MW MF streamwise spectra over NP and SP computed over the full model domain along x and averaged over $+/-25$ km in y km are shown in Figure 14. Colors show Δx from 0.5 (red) to 8 km (black), the latter of which is only marginally non-zero at 70 km, $\lambda_x > 80$ km, and the later times.

MF spectra at both altitudes reveal large variations from earlier to later times among the responses over NP and SP, and for varying Δx. The largest initial responses occur over SP at both altitudes because of its more efficient generation of MWs having $\lambda_x \sim$ 50–80 km and large vertical group velocities (see the inset spectra at lower right in the upper panel of Figure 1). These MWs propagate rapidly into the mesosphere and yield significant MFs at 50 and 70 km from 8 to 9 hr, but exhibit marginal evanescence beginning at $z \sim$ 35–45 km for these λ_x (see Figure 2f of Lund et al., 2020). Smaller $\lambda_x \sim$ 20–40 km over the NP orography are strongly evanescent, hence do not contribute primary MW MF at early times at either altitude.

At the later times (10–12 hr), the MF spectra across NP and SP exhibit negative values from $\lambda_x \sim$ 40–160 km at $z = 50$ km and from $\lambda_x \sim$ 25–160 km at $z = 70$ km. Differences from the earlier spectra at $z = 50$ km are due largely to MWs having larger λ_x and smaller c_{gz} attaining higher altitudes, especially at $\lambda_x \sim$ 80 and 110 km and longer over NP, and a decrease of smaller λ_x MW amplitudes over SP by 10 hr (see Figures 2, 5, and 6).

MF spectra averaged from 10 to 12 hr at $z = 70$ km from $\lambda_x \sim$ 40–160 km have significantly smaller amplitudes than seen at $z = 50$ km for several reasons. There is a smaller initial $U(z) \sim 110$ ms^{-1} and further reduced $U(z)$ at 10 hr over and in the lee of NP and SP at $z = 70$ km relative to those at $z = 50$ km due to pseudo-momentum deposition at earlier times. Additionally, because MW intrinsic phase speeds vary as $c_i \sim -U_h$ (neglecting SA dynamics), $u' \sim c_i$ is required for breaking, $w' \sim u'\lambda_z/\lambda_x$, and MW $|<u'w'>|$ is significantly smaller at 70 than at 50 km for all λ_x.

MFs at $\lambda_x <$ 25–40 km at $z = 70$ km having negative MFs are unlikely to be initial MWs because there is little evidence for such at $z = 50$ km over either peak even at late times. They are more likely evidence of SGWs excited by MW breaking at lower altitudes and earlier times having negative phase speeds with respect to the local mean flow, hence with negative MFs and exhibiting refraction and secondary breaking above.

Surprisingly, the MF spectrum over NP for 8–9 hr is significantly larger for $\Delta x = 2$ km than for $\Delta x = 0.5$ or 1 km. Inspection of the detailed flow accounting for MW breaking over this interval reveals that coarser 2 km resolution causes the instabilities accounting for breaking to revert from smaller-scale, 3-D vortex rings resolved for $\Delta x = 0.5$ and 1 km to a single, larger-scale 2-D (nonphysical) spanwise-aligned vortex that is anticipated for breaking dynamics at much smaller (and more poorly resolved) *Re*. This 2-D vortex enables both larger MW amplitudes and MF spectral amplitudes by decreasing dissipation over the central portion of this interval (see the much smaller vortex cores enabled for $\Delta x = 0.5$ km in Figure 6 of Lund et al., 2020).

6. Implications for Global Modeling of GW Dynamics and Responses

Results presented above reveal dramatic impacts of decreasing resolution on the fidelity of modeling MW and secondary wave dynamics and large-scale responses extending into the stratosphere and mesosphere accompanying increasing eastward flow over the Southern Andes terrain. Comparisons of the CGCAM simulation results for varying horizontal resolutions from $\Delta x = 0.5$–8 km reveal that resolutions of $\Delta x = 0.5$–2 km yield MW, SGW, and large-scale fields that are in quite good agreement in most respects. However, responses in the more computationally efficient simulation with $\Delta x = 2$ km are somewhat weaker, less extensive, and delayed relative to those for $\Delta x = 0.5$ and 1 km, but the coarser resolution does capture most of the diverse responses from small MW breaking scales to large-scale induced ΔU_h in the stratosphere and mesosphere.

Results for $\Delta x = 4$ km are quantitatively weaker and more restricted than those for $\Delta x = 0.5$–2 km and are considered to be unacceptable approximations for both the MW and the larger-scale responses. The $\Delta x = 8$ km case,

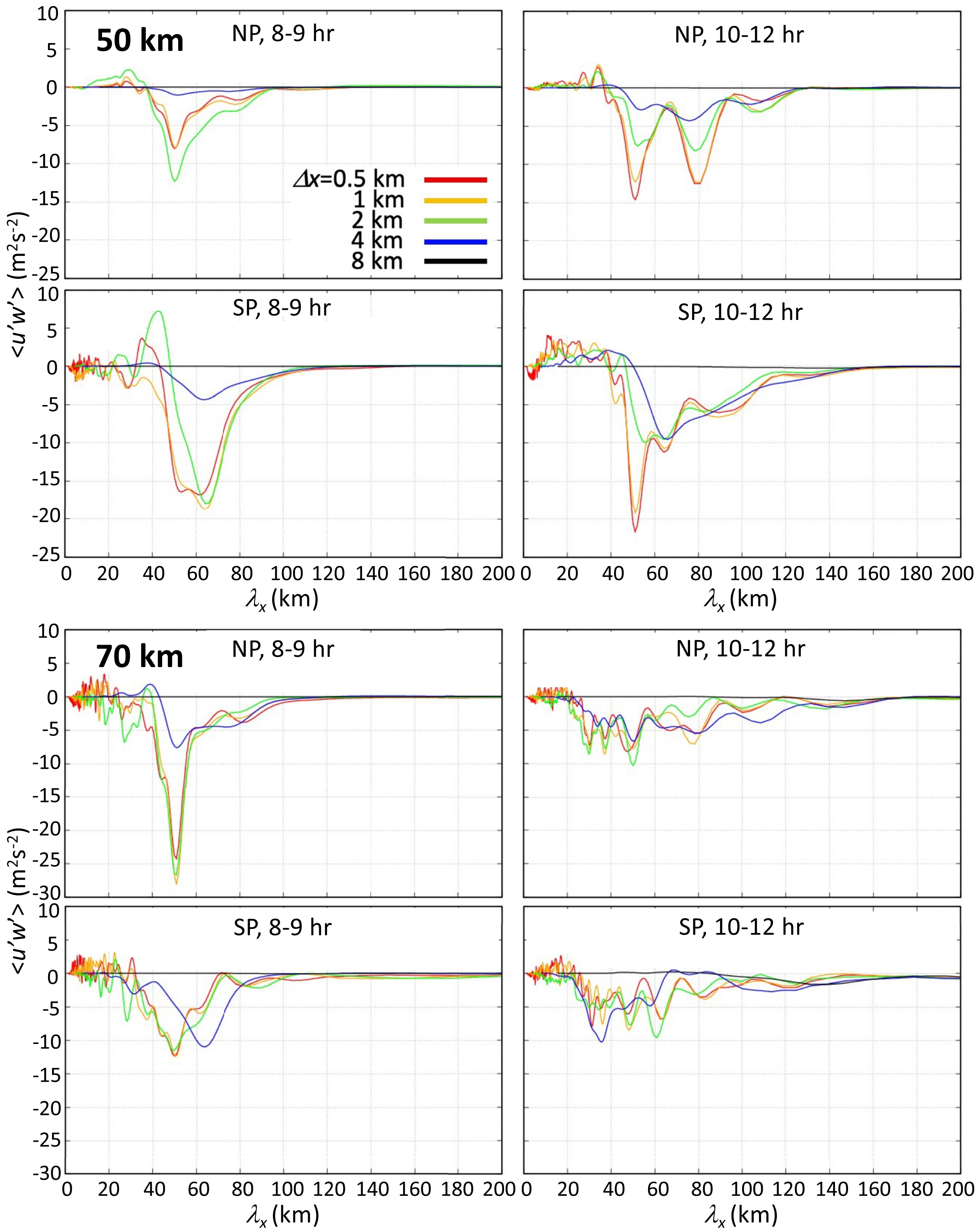

Figure 14. Streamwise $<u'w'>$ spectra at 50 and 70 km (upper and lower 4-panel sets). Those for NP (SP) are shown at top (bottom) averaged from 8 to 9 (10–12) hr at left (right) for each set. Line codes are shown in the upper left panel.

near those of the NWP GFS (12.5 km) and IFS (9 km), bears little resemblance to the fields for smaller Δx. The failure to approximate the initial MW responses for $\Delta x = 8$ km is due to both the exclusion of scales smaller than the Nyquist mode at 16 km and to the large phase errors present from 16 km to the most energetic GW mode of ~50 km. The latter effect is present in all finite-difference and FV schemes, with the severity of these errors for the smallest resolved scales being only weakly dependent on the scheme order of accuracy (see Appendix A). Thus, even if an operational model detects apparent GW motions spanning 2–6 grid cells, the dynamics of these scales will be severely compromised by phase (and perhaps dissipative) errors.

Also performed, but not discussed above, were cases having isotropic central resolutions of 1, 2, and 4 km. These revealed further response degradations relative to the corresponding cases with $\Delta x = 0.5$ km, which we also attribute to worsening resolution of MW instability dynamics and their influences at higher altitudes. These collective results suggest that global or large-scale models must achieve horizontal resolution better than 4 km, and vertical resolution of 0.5 km or better, with higher resolution required where weaker mean winds constrain GW and instability scales, in order to approximate realistic results without significant reliance on parameterizations of larger-scale responses to MW dynamics, secondary wave generation, and mean-flow interactions.

Over the next decade, global cloud-resolving (and terrain-resolving) NWP models will be targeting forecasts at horizontal resolutions of ~1.5–3 km or better (e.g., Stephan et al., 2019; Wedi et al., 2020) and doubling vertical resolution from the surface to 0.01 hPa. The CGCAM simulations discussed above provide quantitative, and complementary, guidance on the horizontal resolution required to adequately describe more general multi-scale nonlinear GW dynamics in the next generation of global NWP models. Specifically, the current CGCAM results confirm that simulations by global and regional models must achieve effective resolution better than 4 km, and preferably ~2 km or better to resolve key GW dynamics and their induced larger-scale influences on the large-scale circulation, mixing, and transport from the troposphere into the mesosphere.

High-resolution simulations promise to avoid the significant reliance on vertical column sub-grid parameterizations of MWs employed in many current NWP and Climate models. These parameterizations do not account for the nonlinearity, intermittency, and transience of MW dynamics and responses, nor the generation and influences of SGWs. Rather, they typically employ parameterizations relying on linear theory and discrete or idealized GW spectral forms (Kim et al., 2003). Our results provide quantitative insights into, and confirmation of, significant deficiencies, especially large-scale circulation biases, in current parameterizations of orographic GW drag (GWD; Sandu et al., 2019; Strube et al., 2021; van Niekerk et al., 2020; Vosper et al., 2019) and of non-orographic GWD (Geller et al., 2013; Müller et al., 2018; Stephan et al., 2019).

Specific examples include the following:

1. vertical-column GWD schemes cannot describe realistic MW/GW responses that extend several hundred km downstream, upstream, and laterally from the surface into the MLT,
2. quasi-stationary GWD parameterizations assuming instantaneous responses at higher altitudes cannot account for responses that may be delayed by several or many hours,
3. current GWD schemes rely on assumptions of linear, slowly varying MW/GW amplitudes and pseudo-momentum deposition that are inconsistent with MW/GW amplitude variability driven by strong nonlinear dynamics and intermittent breaking, and
4. slow, systematic interactions among superposed, resolved MWs and other GWs cannot account for SGW generation at smaller spatial scales accompanying either local SA dynamics or intermittent breaking and induced amplitude modulations.

Early efforts to address these parameterization needs by approximating nonlinear influences on the spectral character of the GW field (e.g., Fritts & VanZandt, 1993; Hines, 1997; Warner & McIntyre, 1996) have continued to the present (Liu, 2019). Other approaches addressing "gray zone" dynamics ($\Delta x \sim 2$–32 km) seeking to relate unresolved responses to resolved surface stresses appear to have significant promise (Vosper et al., 2016, 2019). However, inter-model comparisons of current orographic, convective, and storm track source descriptions reveal significant deficiencies in their GW responses, variations in altitude, and a general inability to approximate higher-resolution fields via parameterization (Stephan et al., 2019; van Niekerk et al., 2020).

CGCAM and other models using ~2 km or better resolution are able to describe these "gray zone" dynamics with reasonable fidelity. Such studies enable quantification of a diversity of MW and more general GW dynamics, including GW instabilities, amplitude reductions, intermittency, and SGW generation extending into the stratosphere and above (Doyle et al., 2005; Fritts et al., 2021, 2018; Heale et al., 2019; Lund et al., 2020; Mixa et al., 2021; Vosper, 2015; Vosper et al., 2016, 2019). The local responses can provide guidance for improved sub-grid-scale parameterizations, especially as they extend to even higher resolutions and higher effective Reynolds numbers. CGCAM simulations of SGW generation in regions of strong GW mean-flow interactions and breaking (Dong et al., 2020, 2021; Fritts et al., 2020) specifically highlight the need to describe their influences, given their ubiquitous sources and strong responses from the troposphere into the MLT.

Of these dynamics, SGW generation and responses including nonlinear influences are potentially the most important and least studied to date. Accounting for all SGW dynamics and responses requires a high-resolution mesoscale model able to describe emerging nonlinear GW/mean-flow interactions yielding "self-acceleration" (SA) dynamics that account for GW packet stalling, local body forcing, and larger-scale SGW generation. Larger-scale SA dynamics do not rely on GW instabilities and breaking, which are instead by-products of the larger-scale SA dynamics. Strong MW responses and breaking in the troposphere and lower stratosphere may prove to be the strongest sources of larger- and smaller-scale SGWs at higher altitudes due to their widespread sources and especially their potential to achieve large amplitudes and breaking at low altitudes and small horizontal scales (see the MW and SA references cited in the Introduction). Other GW sources will surely also contribute to SGW generation, but potentially more weakly due to often larger scales and their expected attainment of large amplitudes at higher altitudes.

While high-resolution regional and global simulations achieving horizontal resolutions of $\Delta x \sim 2$ km are likely to approximate well the large-scale dynamics extending to high altitudes, un-resolved smaller-scale dynamics will continue to require parameterizations where resolutions are coarse and/or GW scales are small. This is due to multiple factors, including the following: (a) lack of sufficient initial conditions, (b) sensitive dependence of emerging GWs and instabilities on small initial optimal perturbations, (c) nonlinearities driving interactions and instabilities, (d) transience and intermittency due to GW breaking or local KH shear instabilities that drive GW amplitudes to values often much smaller than incipient overturning amplitudes, and (e) local influences of turbulence and mixing that are not adequately described or understood at present in the atmosphere or oceans (Dimotakis, 2005; Gregg et al., 2018; Mashayek et al., 2017). This is, in part, because imposed GW amplitude constraints imply much smaller effective GW Reynolds numbers, $Re_{eff}=(c-U)\lambda_z/\nu_{eff}=N\lambda_z^2/2\pi\nu_{\mathrm{eff}}$, for an assumed effective turbulence kinematic viscosity, ν_{eff}, and much larger implied instability scales, where they may be resolved for artificially small Re_{eff}. Such responses also imply significant suppression of, or lack of, SGW generation and much smaller transient reductions of GW amplitudes, and associated modulation of GW breaking intermittency and associated MFs.

The above discussion focused entirely on varying horizontal resolution. Multiple previous studies have also emphasized the importance of high vertical resolution. Hence, we have also performed additional simulations for isotropic resolution of 1 and 2 km. These reveal very significant additional degradation relative to the corresponding fields having $\Delta x = 0.5$ km. These results are provided as Supplemental Materials files, which compare the two responses in all the fields displayed above. As noted above, Appendix A provides a detailed discussion of the implications of finite-difference resolutions for representation of these and other GW dynamics.

7. Conclusions

CGCAM simulations of MW dynamics over the Southern Andes performed for varying horizontal resolution reveal a systematic degradation of responses as horizontal resolution, Δx (and Δy), coarsens from 0.5 to 8 km. These include (a) decreasing regions undergoing instabilities and breaking, (b) decreasing resolution of the MW instability dynamics accounting for breaking, (c) weakening and disappearance of SGW and AW generation as MW breaking weakens and fails to be resolved, (d) shrinking and weakening of the induced mean-flow decelerations, and (e) weakening and narrowing downstream wakes of decelerated U.

These multi-scale simulations provide guidance on resolutions likely to be required for mesoscale or global models intended to account for MW and more general GW generation, propagation, and transports of pseudo-momentum and energy into the stratosphere and mesosphere, and potential generation of SGWs extending into the MLT. More importantly, perhaps, because most global models will not enable such extreme resolutions, the results presented here may provide guidance for parameterization of the various responses at higher altitudes because they describe both the responses requiring description and the dynamics that provide the basis for parameterizations of these responses. They also provide motivations for developments of nesting capabilities in GCMs able to couple to high-resolution local simulations.

Appendix A: Finite-Difference Errors in Numerical Simulations

Most numerical simulations are affected by two sources of error: (a) representation error and (b) numerical error. Representation error stems from the fact that the computational mesh only supports a finite number of scales, ranging from the computational box dimension (L) to twice the grid spacing (2Δ), whereas numerical error arises from the discrete approximations to the derivative operators in the conservation laws. As the mesh is coarsened the representation error damages the solution through the removal of important scales of motion. For example, the shorter wavelength components of the primary wave packet in our simulations are absent at the coarser resolutions and important instability scales are also missing. Numerical error, on the other hand, preferentially upsets the dynamics of the smallest resolved scales. Using information contained in Moin (2001), the relative error in phase speed for a 1-D linear wave equation model problem for any properly constructed finite difference or finite volume scheme can be written as:

$$e = 1 - \left(\frac{\lambda}{2\pi\Delta}\right) \sum_{n=1}^{\mathrm{int}\left(\frac{N+1}{2}\right)} A_n \sin\left(\frac{2\pi n\Delta}{\lambda}\right)$$

where λ is the wavelength, Δ is the mesh spacing, N is the order of accuracy, and int() is the integer truncation. The coefficients A_n for second through sixth order schemes are shown in Table A1. Even-ordered (centered) schemes only contain phase error, whereas odd-ordered (skewed) schemes also contain dissipative errors. While dissipative errors are especially harmful for wave and turbulent phenomena, we shall not discuss these here since we have used a centered scheme. A Taylor series analysis of the error equation above for well-resolved waves ($\Delta/\lambda \rightarrow 0$) reveals the scheme order of accuracy, whereas an evaluation at the Nyquist limit ($\Delta/\lambda \rightarrow 1/2$) shows the astonishing result that ALL discrete schemes have 100% phase error for the smallest resolved scale. This latter result is significant since it indicates that increasing the order of accuracy will improve the situation very little for marginally resolved scales.

The foregoing analysis can be used to loosely extrapolate the results obtained with our 2nd order scheme to those of higher order. To do this we simply determine the mesh spacing for a higher order scheme that produces the same phase error experienced by our scheme, when using the most energetic horizontal wavelength of $\lambda_h = 50$ km. The results are shown in Table A2, where Δ_{eq} is the equivalent mesh spacing yielding the same phase error as the 2nd order scheme. This table shows that, while considerably coarser meshes could potentially be used by higher order schemes in the fine spacing regime, the gains erode steadily as the mesh is coarsened, and show only marginal improvement at a spacing of 16 km. We should caution that this analysis ignores representation error, which can also have serious impacts on the solution at coarser resolution. Thus, it appears unrealistic to think that a simulation using a 6th order method with a spacing of 6.9 km would produce results equivalent to what we have obtained with a spacing of 1 km.

It can also be shown that the phase error results in a reduction in both the GW phase speed and in the vertical group velocity. At the coarser resolutions, this effect introduces a pronounced time delay in the solutions as it takes longer for the MW packet shaped by the wind ramping procedure to propagate to higher altitudes.

Table A1
Error Analysis Coefficients for Central-Difference Schemes of Various Orders

Order	A_1	A_2	A_3
1,2	1	0	0
3,4	4/3	−1/6	0
5,6	3/2	−3/10	1/30

Table A2
Higher-Order Scheme Mesh Spacings Giving Error Equal to the Second Order Scheme

Order	1,2	3,4	5,6
Spacing (km)	D	D_{eq}	D_{eq}
	1	4.25	6.90
	2	6.05	8.83
	4	8.70	11.4
	8	12.7	15.0
	16	19.0	20.3

Data Availability Statement

Supplemental Materials include high-resolution figures and https://zenodo.org/deposit/5815467 hosts the figures and the data files needed to recreate the figures.

Acknowledgments
Research described here was performed under AFOSR grant FA9550-18-0009, NASA grants 80NSSC20K0170 and 80GSFC18C0007, and NSF grants AGS-1647354 and AGS-2131350 cited in GEMS. The authors thank the DoD HPCMP for computational resources that enabled this modeling study. Contributions by VY were supported by the NASA/GSFC Cooperative Agreement 80NSSC21M0180 to Catholic University of America. The authors also thank two anonymous reviewers for multiple comments that improved the paper.

References

Achatz, U. (2005). On the role of optimal perturbations in the instability of monochromatic gravity waves. *Physics of Fluids*, *17*(9), 094107. https://doi.org/10.1063/1.2046709

Achatz, U. (2007). The primary nonlinear dynamics of modal and nonmodal perturbations of monochromatic inertia-gravity waves. *Journal of the Atmospheric Sciences*, *64*(1), 74–95. https://doi.org/10.1175/JAS3827.1

Andreassen, O., Hvidsten, P. O., Fritts, D. C., & Arendt, S. (1998). Vorticity dynamics in a breaking gravity wave. Part 1. Initial instability evolution. *Journal of Fluid Mechanics*, *367*, 27–46. https://doi.org/10.1017/S0022112098001645

Andreassen, O., Wasberg, C. E., Fritts, D. C., & Isler, J. R. (1994). Gravity wave breaking in two and three dimensions: 1. Model description and comparison of two-dimensional evolutions. *Journal of Geophysical Research*, *99*(D4), 8095–8108. https://doi.org/10.1029/93JD03435

Becker, E., & Vadas, S. L. (2018). Secondary gravity waves in the winter mesosphere: Results from a high-resolution global circulation model. *Geophysical Research Letters*, *123*, 2605–2627. https://doi.org/10.1002/2017JD027460

Becker, E., & Vadas, S. L. (2020). Explicit global simulation of gravity waves in the thermosphere. *Journal of Geophysical Research: Space Physics*, *125*, e2020JA028034. https://doi.org/10.1029/2020JA028034

Bourget, B., Dauxois, T., Joubaud, S., & Odier, P. (2013). Experimental study of parametric subharmonic instability for internal plane waves. *Journal of Fluid Mechanics*, *723*, 1–20. https://doi.org/10.1017/jfm.2013.78

Dimotakis, P. E. (2005). Turbulent mixing. *Annual Review of Fluid Mechanics*, *37*, 329–356. https://doi.org/10.1146/annurev.fluid.36.050802.122015

Dong, W., Fritts, D. C., Lund, T. S., Wieland, S. A., & Zhang, S. (2020). Self-acceleration and instability of gravity wave packets: 2. Two-dimensional packet propagation, instability dynamics, and transient flow responses. *Journal of Geophysical Research: Atmospheres*, *125*, e2019JD030691. https://doi.org/10.1029/2019JD030691

Dong, W., Fritts, D. C., Thomas, G. E., & Lund, T. S. (2021). Modeling responses of polar mesospheric clouds to gravity wave and instability dynamics and induced large-scale motions. *Journal of Geophysical Research: Atmospheres*, *126*, e2021JD034643. https://doi.org/10.1029/2021JD034643

Doyle, J. D., Shapiro, M. A., Jiang, Q., Bartels, D. L. (2005). Large-amplitude mountain waves over Greenland. *Journal of the Atmospheric Sciences*, *62*, 3106–3126. https://doi.org/10.1175/jas3528.1

Ern, M., Preusse, P., & Warner, C. D. (2006). Some experimental constraints for spectral parameters used in the Warner and McIntyre gravity wave parameterization scheme. *Atmospheric Chemistry and Physics*, *6*, 4361–4381. https://doi.org/10.5194/acp-6-4361-2006

Felten, F. N., & Lund, T. S. (2006). Kinetic energy conservation issues associated with the collocated mesh scheme for incompressible flow. *Journal of Computational Physics*, *215*, 465–484. https://doi.org/10.1016/j.jcp.2005.11.009

Fritts, D. C., & Alexander, M. J. (2003). Gravity wave dynamics and effects in the middle atmosphere. *Reviews of Geophysics*, *41*, 1003. https://doi.org/10.1029/2001RG000106

Fritts, D. C., Dong, W., Lund, T. S., Wieland, S., & Laughman, B. (2020). Self-acceleration and instability of gravity wave packets: 3. Three-dimensional packet propagation, secondary gravity waves, momentum transport, and transient mean forcing in tidal winds. *Journal of Geophysical Research: Atmospheres*, *125*, e2019JD030692. https://doi.org/10.1029/2019JD030692

Fritts, D. C., Laughman, B., Lund, T. S., & Snively, J. B. (2015). Self-acceleration and instability of gravity wave packets: 1. Effects of temporal localization. *Journal of Geophysical Research: Atmospheres*, *120*, 8783–8803. https://doi.org/10.1002/2015JD023363

Fritts, D. C., Lund, T. S., Lund, A. C., & Yudin, V. (2022). Impacts of limited model resolution on the representation of mountain wave and secondary wave dynamics in local and global models. Part 2: Mountain wave and secondary wave evolutions in the thermosphere, *Journal of Geophysical Research*.

Fritts, D. C., Lund, T. S., Wan, K., & Liu, H.-L. (2021). Numerical simulation of mountain waves over the southern Andes. Part 2: Momentum fluxes, mean-flow accelerations, and gravity-wave/tidal interactions. *Journal of the Atmospheric Sciences*, 3069–3088. https://doi.org/10.1175/JAS-D-20-0207.1

Fritts, D. C., & Rastogi, P. K. (1985). Convective and dynamical instabilities due to gravity wave motions in the lower and middle atmosphere: Theory and observations. *Radio Science*, *20*, 1247–1277. https://doi.org/10.1029/rs020i006p01247

Fritts, D. C., & Vadas, S. L. (2008). Gravity wave penetration into the thermosphere: Sensitivity to solar cycle variations and mean winds. *Annals of Geophysics*, *26*, 3841–3861. https://doi.org/10.5194/angeo-26-3841-2008

Fritts, D. C., & VanZandt, T. E. (1993). Spectral estimates of gravity wave energy and momentum fluxes, I. Energy dissipation, acceleration, and constraints. *Journal of the Atmospheric Sciences*, *50*(22), 3685–3694. https://doi.org/10.1175/1520-0469(1993)050<3685:seogwe>2.0.co;2

Fritts, D. C., Vosper, S. B., Williams, B. P., Bossert, K., Plane, J. M. C., Taylor, M. J., et al. (2018). Large-amplitude mountain waves in the mesosphere accompanying weak cross-mountain flow during DEEPWAVE Research Flight RF22. *Journal of Geophysical Research: Atmospheres*, *123*. https://doi.org/10.1029/2017JD028250

Fritts, D. C., Wang, L., Baumgarten, G., Miller, A. D., Geller, M. A., Jones, G., et al. (2017). High-resolution observations and modeling of turbulence sources, structures, and intensities in the upper mesosphere. *Journal of Atmospheric and Solar-Terrestrial Physics*, *162*, 57–78. https://doi.org/10.1016/j.jastp.2016.11.006

Fritts, D. C., Wang, L., Werne, J., Lund, T., & Wan, K. (2009). Gravity wave instability dynamics at high Reynolds numbers. Part II: Turbulence evolution, structure, and anisotropy. *Journal of the Atmospheric Sciences*, *66*(5), 1149–1171. https://doi.org/10.1175/2008JAS2727.1

Garcia, R. R., & Boville, B. A. (1994). "Downward control" of the mean meridional circulation and temperature distribution of the polar winter stratosphere. *Journal of the Atmospheric Sciences*, *51*(15), 2238–2245. https://doi.org/10.1175/1520-0469(1994)051<2238:cotmmc>2.0.co;2

Geller, M. A., & Coauthors (2013). A comparison between gravity wave momentum fluxes in observations and climate models. *Journal of Climate*, *26*, 6383–6405. https://doi.org/10.1175/JCLI-D-12-00545.1

Germano, M., Piomelli, U., Moin, P., & Cabot, W. H. (1991). A dynamic subgrid-scale eddy viscosity model. *Physics of Fluids A*, *3*(7), 1760–1765. https://doi.org/10.1063/1.857955

Gregg, M. C., D'Asaro, E. A., Riley, J. J., & Kunze, E. (2018). Mixing efficiency in the ocean. *Annual Review of Marine Science*, *10*, 443–473. https://doi.org/10.1146/annurev-marine-121916-063643

Hastings, D. A., Dunbar, P. K., Elphingstone, G. M., Bootz, M., Murakami, H., Maruyama, H., et al. (Eds.). (1999). *The Global Land One-Kilometer Base Elevation (GLOBE) digital elevation model, version 1.0*. NOAA National Geophysical Data Center. Retrieved 15 September 2017 from https://www.ngdc.noaa.gov/mgg/topo/globe.html

Heale, C. J., Snively, J. B., Bhatt, A. N., Hoffmann, L., Stephan, C. C., & Kendall, E. A. (2019). Multilayer observations and modeling of thunderstorm-generated gravity waves over the Midwestern United States. *Geophysical Research Letters*, *46*(23), 14164–14174. https://doi.org/10.1029/2019GL085934

Hines, C. O. (1960). Internal atmospheric gravity waves at ionospheric heights. *Canadian Journal of Physics*, *38*, 1441–1481. https://doi.org/10.1139/p60-150

Hines, C. O. (1997). Doppler-spread parameterization of gravity-wave momentum deposition in the middle atmosphere, 1. Basic formulation. *Journal of Atmospheric and Solar-Terrestrial Physics*, *59*(4), 371–386. https://doi.org/10.1016/S1364-6826(96)00079-X

Holton, J. R. (1982). The role of gravity wave-induced drag and diffusion in the momentum budget of the mesosphere. *Journal of the Atmospheric Sciences*, *39*, 791–799. https://doi.org/10.1175/1520-0469(1982)039<0791:trogwi>2.0.co;2

Kim, Y.-J., Eckermann, S. D., & Chun, H.-Y. (2003). An overview of the past, present, and future gravity-wave drag parameterization for numerical climate and weather prediction models. *Atmosphere-Ocean*, *41*, 65–98. https://doi.org/10.3137/ao.410105

Lindzen, R. S. (1981). Turbulence and stress owing to gravity wave and tidal breakdown. *Journal of Geophysical Research*, *86*, 9707–9714. https://doi.org/10.1029/jc086ic10p09707

Liu, H.-L. (2016). Variability and predictability of the space environment as related to lower atmosphere forcing. *Space Weather*, *14*, 634–658. https://doi.org/10.1002/2016SW001450

Liu, H.-L. (2019). Quantifying gravity forcing using the scale invariance. *Nature Communications*, *10*, 2605. https://doi.org/10.1038/s41467-019-10527-z

Liu, H.-L., McInerney, J. M., Santos, S., Lauritzen, P. H., Taylor, M. A., & Pedatella, N. M. (2014). Gravity waves simulated by high-resolution whole atmosphere community climate model. *Geophysical Research Letters*, *41*(24), 9106–9112. https://doi.org/10.1002/2014GL062468

Lund, T. S., Fritts, D. C., Wan, K., Laughman, B., & Liu, H. (2020). Numerical simulation of mountain waves over the Southern Andes. Part 1: Mountain wave and secondary wave character, evolutions, and breaking. *Journal of the Atmospheric Sciences*, *77*, 4337–4356. https://doi.org/10.1175/JAS-D-19-0356.1

Mashayek, A., Salehipour, H., Bouffard, D., Caulfield, C. P., Ferrari, R., Nikurashin, M., et al. (2017). Efficiency of turbulent mixing in the abyssal ocean circulation. *Geophysical Research Letters*, *44*, 6296–6306. https://doi.org/10.1002/2016GL072452

McFarlane, N. A. (1987). The effect of orographically excited gravity wave drag on the general circulation of the lower stratosphere and troposphere. *Journal of the Atmospheric Sciences*, *44*, 1775–1800. https://doi.org/10.1175/1520-0469(1987)044<1775:teooeg>2.0.co;2

Mixa, T., Dornbrack, A., & Rapp, M. (2021). Nonlinear simulations of gravity wave tunneling and breaking over Auckland Island. *Journal of the Atmospheric Sciences*, *78*, 1567–1582. https://doi.org/10.1175/JAS-D-20-0230.1

Moin, P. (2001). *Fundamentals of engineering numerical analysis*. Cambridge University Press.

Moin, P., Squires, K. D., Cabot, W. H., & Lee, S. (1991). A dynamic subgrid-scale model for compressible turbulence and scalar transport. *Physics of Fluids A*, *3*(11), 2746–2757. https://doi.org/10.1063/1.858164

Müller, S. K., Manzini, E., Giorgetta, M. A., Sato, K., & Nasuno, T. (2018). Convectively generated gravity waves in high-resolution models of tropical dynamics. *Journal of Advances in Modeling Earth Systems*, *10*, 2564–2588. https://doi.org/10.1029/2018MS001390

Palmer, T. L., Shutts, G. J., & Swinbank, R. (1986). Alleviation of a systematic westerly bias in general circulation and numerical weather prediction models through an orographic gravity wave drag parameterization. *Quarterly Journal of the Royal Meteorological Society*, *122*(474), 1001–1039. https://doi.org/10.1002/qj.49711247406

Plougonven, R., & Zhang, F. (2014). Internal gravity waves from atmospheric jets and fronts. *Reviews of Geophysics*, *52*(1), 33–76. https://doi.org/10.1002/2012RG000419

Sandu, I., van Niekerk, A., Shepherd, T. G., Vosper, S. B., Zadra, A., Bacmeister, J., et al. (2019). Impacts of orography on large-scale atmospheric circulation. *npj Climate and Atmospheric Science*, *2*, 10. https://doi.org/10.1038/s41612-019-0065-9

Scinocca, J. F., & Sutherland, B. R. (2010). Self-acceleration in the parameterization of orographic gravity wave drag. *Journal of the Atmospheric Sciences*, *67*, 2537–2546. https://doi.org/10.1175/2010JAS3358.1

Smith, A. K., Garcia, R. R., Marsh, D. R., & Richter, J. H. (2011). WACCM simulations of the mean circulation and trace species transport in the winter mesosphere. *Journal of Geophysical Research: Atmospheres*, *116*, D20. https://doi.org/10.1029/2011JD016083

Stephan, C. C., Strube, C., Klocke, D., Ern, M., Hoffmann, L., Preusse, P., & Schmidt, H. (2019). Intercomparison of gravity waves in global convection-permitting models. *Journal of the Atmospheric Sciences*, *76*, 2739–2759. https://doi.org/10.1175/JAS-D-19-0040.1

Strube, C., Preusse, P., Ern, M., & Riese, M. (2021). Propagation paths and source distributions of resolved gravity waves in ECMWF-IFS analysis fields around the southern polar night jet. *Atmospheric Chemistry and Physics*, *21*, 18641–18668. https://doi.org/10.5194/acp-2021-160

Sutherland, B. R. (2013). The wave instability pathway to turbulence. *Journal of Fluid Mechanics*, *724*, 1–4. https://doi.org/10.1017/jfm.2013.149

vanNiekerk, A., Sandu, I., Zadra, A., Bazil, E., Kanehama, T., Köhler, M., et al. (2020). COnstraining ORographic Drag Effects (COORDE): A model comparison of resolved and parameterized orographic drag. *Journal of Advances in Modeling Earth Systems*, *12*, e2020MS002160. https://doi.org/10.1029/2020ms002160

Vosper, S. B. (2015). Mountain waves and wakes generated by South Georgia: Implications for drag parameterization. *Quarterly Journal of the Royal Meteorological Society*, *141*(692), 2813–2827. https://doi.org/10.1002/qj.2566

Vosper, S. B., Brown, A. R., & Webster, S. (2016). Orographic drag on islands in the NWP mountain grey zone. *Quarterly Journal of the Royal Meteorological Society*, *142*, 3128–3137. https://doi.org/10.1002/qj.2894

Vosper, S. B., vanNiekerk, A., Elvidge, A., Sandu, I., & Beljaars, A. (2019). What can we learn about orographic drag parametrisation from high-resolution models? A case study over the Rocky Mountains. *Quarterly Journal of the Royal Meteorological Society*, *146*, 979–995. https://doi.org/10.1002/qj.3720

Warner, C. D., & McIntyre, M. E. (1996). On the propagation and dissipation of gravity wave spectra through a realistic middle atmosphere. *Journal of the Atmospheric Sciences*, *53*, 3213–3235. https://doi.org/10.1175/1520-0469(1996)053<3213:otpado>2.0.co;2

Wedi, N. P., Polichtchouk, I., Dueben, P., Anantharaj, V. G., Bauer, P., Boussetta, S., et al. (2020). A baseline for global weather and climate simulations at 1 km resolution. *Journal of Advances in Modeling Earth Systems*, *12*, e2020MS002192. https://doi.org/10.1029/2020MS002192

White, F. M. (1974). *Viscous fluid flow*. New York: McGraw-Hill.

Witt, G. (1962). Height, structure and displacement of noctilucent clouds. *Tellus*, *14*(1), 1–18. https://doi.org/10.3402/tellusa.v14i1.9524